

Weak Polarized Electron Scattering

JENS ERLER

*PRISMA Cluster of Excellence & Mainz Institute for Theoretical Physics,
Johannes Gutenberg University, D-55099 Mainz, Germany*

*Permanent address: Departamento de Física Teórica, Instituto de Física,
Universidad Nacional Autónoma de México, México D.F. 04510, México*

CHARLES J. HOROWITZ

*Department of Physics and Nuclear Theory Center, Indiana University,
Bloomington, IN 47405, USA*

SONNY MANTRY

*High Energy Division, Argonne National Laboratory, Argonne, IL 60439
Department of Physics and Astronomy, Northwestern University,
Evanston, IL 60208*

PAUL A. SOUDER

Physics Department, Syracuse University, Syracuse, New York 13244

Key Words Weak Neutral Currents, Parton Distributions, Neutron Stars, Physics
Beyond the Standard Model

Abstract

Scattering polarized electrons provides an important probe of the weak interactions. Precisely measuring the parity-violating left-right cross section asymmetry is the goal of a number of experiments recently completed or in progress. The experiments are challenging, since A_{LR} is small, typically between 10^{-4} and 10^{-8} . By carefully choosing appropriate targets and kinematics, various pieces of the weak Lagrangian can be isolated, providing a search for physics beyond the Standard Model. For other choices, unique features of the strong interaction are studied, including the radius of the neutron density in heavy nuclei, charge symmetry violation, and higher twist terms. This article reviews the theory behind the experiments, as well as the general techniques used in the experimental program.

CONTENTS

INTRODUCTION	3
<i>Overview</i>	3
<i>Electroweak Physics</i>	4
<i>Hadronic and Nuclear Physics</i>	8
EXPERIMENTAL ISSUES	8
<i>Introduction</i>	8
<i>Brief Descriptions of Selected Experiments</i>	8
<i>Precision of PVES Experiments</i>	13
THEORETICAL ISSUES	17
<i>Effective Couplings</i>	17
<i>Radiative Corrections</i>	18
<i>Theoretical Uncertainties</i>	21
HADRONIC STRUCTURE	26

Higher Twist Effects 27

Charge Symmetry Violation 29

Extracting the d/u Ratio of Parton Distribution Functions 32

NUCLEAR PHYSICS 33

Nuclear Formalism 34

Neutron Skins and the Symmetry Energy 36

Neutron Skins and Astrophysics 37

Nuclear Experiments 39

PROBING NEW PHYSICS 41

Beyond the SM Amplitudes and New Physics Scales 41

Leptophobic Z's 45

Dark Z 47

CONCLUSIONS 49

1 INTRODUCTION

1.1 Overview

In 1978, SLAC experiment E122 (1,2) published the observation of parity violation in the deep inelastic scattering of polarized electrons from deuterium. It settled the issue as to whether or not the then recently discovered weak neutral currents were parity-violating and led to the universal acceptance of the Standard Model (SM). The experiment also demonstrated that parity violation in electron scattering (PVES) is a viable tool for particle and nuclear physics.

In the following 35 years, many new PVES experiments were performed or are planned at various laboratories around the world, including SLAC, Mainz, MIT-Bates, and JLab. The goals of the new experiments included searching for non-

zero strange elastic form factors (3), measuring the weak mixing angle, $\sin^2 \theta_W$, at low energies (4), measuring a set of electroweak (EW) couplings, measuring the radius R_n of the distribution of neutrons in heavy nuclei, searching for charge symmetry violation (CSV) at the quark level, and measuring higher-twist effects in deep inelastic scattering (DIS). The first two topics have been the subject of previous reviews (3,4); here we will focus on the other topics.

The basic idea of PVES is to measure the parity-violating EW asymmetry,

$$A_{LR} = \frac{\sigma_L - \sigma_R}{\sigma_L + \sigma_R}, \quad (1)$$

where σ_L (σ_R) is the cross section for the scattering of electrons with left (right) helicity. The leading order effect arises from an interference between photon and Z exchange, resulting in small asymmetries proportional to the four momentum transfer Q^2 and also to the EW couplings. Values of A_{LR} in the range from 10^{-4} to 10^{-8} can be measured with good accuracy. By selecting optimal kinematics and targets, the wide variety of physics mentioned above can be accessed.

A useful feature of A_{LR} is that in the ratio a number of experimental uncertainties cancel, such as those due to target thickness and the solid angle. Some possible theoretical uncertainties, such as elastic form factors, also cancel. The kinematics of the various experiments are chosen either so that unknown hadronic effects cancel, probing EW physics, or so that the hadronic effects remaining are of interest and cannot be measured by other techniques.

1.2 Electroweak Physics

An efficient way to represent the sensitivities of different experiments and observables to the underlying EW physics, including possible new physics beyond the SM, is to use the language of a low-energy effective field theory in a way de-

scribed in Section 3. The parity-violating (PV) part of the neutral-current (NC) interactions of charged fermions with electrons is

$$\mathcal{L}_{\text{NC}}^{ef} = \frac{\bar{e}\gamma^\mu\gamma^5 e}{2v^2} \left(\sum_{q=u,d} g_{AV}^{eq} \bar{q}\gamma_\mu q + \frac{1}{2} g_{AV}^{ee} \bar{e}\gamma_\mu e \right) + \frac{\bar{e}\gamma^\mu e}{2v^2} \sum_{q=u,d} g_{VA}^{eq} \bar{q}\gamma_\mu\gamma^5 q, \quad (2)$$

where $v = (\sqrt{2}G_F)^{-1/2} = 246.22$ GeV and G_F is the Fermi constant. The EW coefficients are real-valued and at the SM tree level given by

$$g_{AV}^{eu} = -\frac{1}{2} + \frac{4}{3} \sin^2 \theta_W, \quad g_{AV}^{ed} = \frac{1}{2} - \frac{2}{3} \sin^2 \theta_W, \quad (3)$$

$$g_{AV}^{ee} = g_{VA}^{ed} = -g_{VA}^{eu} = \frac{1}{2} - 2 \sin^2 \theta_W. \quad (4)$$

We now briefly review how these couplings are extracted experimentally.

Currently, the most precise determination of any combination derives from observations (5) of atomic parity violation (APV), most notably in ^{133}Cs where one also obtained (6,7) the best understanding of atomic structure (8) which is crucial for the interpretation in terms of EW physics. The result,

$$188 g_{AV}^{eu} + 211 g_{AV}^{ed} = 36.35 \pm 0.21, \quad (5)$$

is 1.5σ lower than the SM prediction of 36.66. In the future, one may constrain different linear combinations by studying neutron rich nuclei like Fr or Ra, or by considering isotope ratios in which atomic physics uncertainties cancel.

Note that we are using the notation introduced in Reference (9). More familiar are the so-called weak charges, Q_W , which at the tree level are also given by the coherent sum of the corresponding quark couplings (as in Equation 5), but multiplied by a factor of -2 and with a different set of radiative corrections applied. This is indicated by the use of C_{1q} and C_{2q} in place of g_{AV}^{eq} and g_{VA}^{eq} . Our notation serves as a reminder that corrections have been applied (see Section 3.1) allowing direct comparison and combination of the couplings when extracted from different observables, experiments, and kinematic conditions.

PVES offers an alternative to APV and the possibility to cross-examine Equation 5 with entirely different experimental and theoretical challenges and uncertainties. E.g., the Qweak Collaboration (10) has measured the left-right asymmetry (11) in elastic polarized ep scattering, $\vec{e}^- p \rightarrow e^- p$,

$$A_{LR}^{ep} \equiv \frac{d\sigma_L - d\sigma_R}{d\sigma_L + d\sigma_R} = -\frac{s}{v^2} \frac{g_{AV}^{ep}}{4\pi\alpha} [y + \mathcal{O}(y^2)] \mathcal{F}_{\text{QED}}^{ep}(Q^2, y), \quad (6)$$

where $s = Q^2/y$ is the center-of-mass energy, α the EM fine structure constant, and $\mathcal{F}_{\text{QED}}^{ep}(Q^2, y)$ is a QED correction factor. Here and in the following, y is the fractional energy transfer from the electrons to the hadrons which is perturbatively small for Qweak kinematics, $y \approx 0.0082$, and will be smaller yet for the experiment at the MESA facility in Mainz. The analysis of the Qweak commissioning data (about 4% of the total) translates into the constraint,

$$2g_{AV}^{eu} + g_{AV}^{ed} = -0.032 \pm 0.006, \quad (7)$$

to be compared to SM prediction of -0.0355 . The final result is expected to be four times as precise, and even greater precision will be possible in Mainz. If additionally elastic scattering off isoscalar nuclei like ^{12}C was used to extract $g_{AV}^{ep} + g_{AV}^{en}$, one could disentangle g_{AV}^{eu} and g_{AV}^{ed} from PVES alone.

The analogous asymmetry in Møller scattering (12),

$$A_{LR}^{ee} = \frac{s}{v^2} \frac{g_{VA}^{ee}}{4\pi\alpha} \frac{2y(1-y)}{(1-y+y^2)^2} \mathcal{F}_{\text{QED}}^{ee}(Q^2, y), \quad (8)$$

has been obtained by the SLAC-E158 Collaboration (13) from which one can extract (9),

$$g_{AV}^{ee} = 0.0190 \pm 0.0027, \quad (9)$$

while the SM predicts the value 0.0225. The MOLLER Collaboration (14) at Jefferson Lab aims to reduce the uncertainty in g_{AV}^{ee} by a factor of five by taking advantage of the energy upgraded CEBAF.

Deep inelastic PVES (PVDIS) experiments (2,15) are sensitive to the interference of the quark-level amplitudes corresponding to $\mathcal{L}_{\text{NC}}^{ef}$ with photon exchange. Scattering from an isoscalar target provides information on the charge weighted combinations, $2g_{AV}^{eu} - g_{AV}^{ed}$ and $2g_{VA}^{eu} - g_{VA}^{ed}$. In the quark model and in the limit of zero nucleon mass one can write (9) in a simple valence quark approximation,

$$A_{LR}^{\text{DIS}} = -\frac{3}{20\pi\alpha(Q)} \frac{Q^2}{v^2} \left[(2g_{AV}^{eu} - g_{AV}^{ed}) + (2g_{VA}^{eu} - g_{VA}^{ed}) \frac{1 - (1-y)^2}{1 + (1-y)^2} \right]. \quad (10)$$

One has to correct for higher twist effects, CSV, sea quarks, target mass effects, longitudinal structure functions and nuclear effects. Some of these issues are of considerable interest in their own right, and their discussion is deferred to Sections 4 and 5.

The proposed Electron Ion Collider (EIC) (16), currently under study as the next step in exploring the QCD frontier, is a high luminosity ($\sim 10^{33-34} \text{ cm}^2 \text{ s}^{-1}$) machine that will use highly polarized ($\sim 70\%$) electron and nucleon beams with a variable center of mass energy $20 \text{ GeV} < \sqrt{s} < 150 \text{ GeV}$ and a wide variety of nuclear targets. Such a facility will allow further improved precision studies of PVDIS asymmetries. Its wide kinematic range, along with other experiments, will allow one to disentangle various hadronic effects such as CSV or higher twist effects. In turn, it can also allow for more precise extractions of the contact interaction couplings that are sensitive to new physics and the weak mixing angle at different values of Q^2 .

We will return to the EW couplings, their radiative corrections and the associated uncertainties in Section 3.

1.3 Hadronic and Nuclear Physics

As discussed earlier, sound theoretical control over various hadronic effects that contribute to the asymmetries is essential for a reliable interpretation of the EW physics. Alternatively, one can view PVDIS as a probe of the hadronic effects themselves as a means to further our understanding of QCD and nuclear dynamics. Within this context, we discuss some of the important hadronic effects that affect PVDIS asymmetries in Section 4.

We describe elastic PVES from heavy nuclei in Section 5. These experiments can precisely locate neutrons in the nucleus because the weak charge of a neutron is much larger than that of a proton. These experiments target neutron radii that have important implications for nuclear structure, astrophysics and APV.

2 EXPERIMENTAL ISSUES

2.1 Introduction

A large number of PVES experiments have been completed or are in progress. A list is given in **Table 1** which gives a flavor of the variety of both apparatus and physics goals. We will first give a brief description of selected experiments. Then we will discuss general design criteria that apply to all of the experiments.

2.2 Brief Descriptions of Selected Experiments

In the Qweak experiment (10) electrons scattered from a 35 cm long LH₂ target with angles between 5° and 11° and passed through a collimator. They were deflected by a toroid and focussed onto quartz bars that served as Cherenkov detectors. Virtually all of the apparatus for Qweak was custom fabricated.

Table 1: Apparates for selected PV experiments. For magnets, Q (D) refers to quadrupole (dipole).

Experiment	Magnets	Detector	Count	Angles	Physics
SLAC–E122	Dipoles	Pb Glass	No	12°	g_{AV}^{eq}, g_{VA}^{eq}
Mainz	None	Air C	No	146°	g_{AV}^{eq}
MIT–Bates	Q	Lucite C	No	20°	g_{AV}^{eq}
SAMPLE	None	Air C	No	146°	Strange FF
HAPPEX	QQDDQ	Pb-Lucite	No	15°	Strange FF
GØ	Toroid	Scintillator	Yes	20°-50°	Strange FF
Mainz–A4	None	PbF ₂	Yes	30°	Strange FF
SLAC–E158	QQQQ	Cu-Quartz	No	2°	g_{AV}^{ee}
HAPPEX–He	QQDDQ	Cu-Quartz	No	5°	Strange FF
PREX	QQDDQ	Quartz	No	5°	R_n
PREX-II	QQDDQ	Quartz	No	5°	R_n
CREX	QQDDQ	Quartz	No	4°	R_n
JLab–Hall A	QQDDQ	Pb Glass	Yes	19°	g_{VA}^{eq}
Qweak	Toroid	Pb-Quartz	No	5°	g_{AV}^{eq}
MOLLER	Toroid	Quartz	No	1°	g_{AV}^{ee}
SoLID	Solenoid	Package	Yes	22°-35°	g_{VA}^{eq} , CSV, HT
Mainz–P2	Solenoid	Quartz	No	20°	g_{AV}^{eq}
Mainz–C	Solenoid	Quartz	No	40°	g_{AV}^{eq}

By contrast, the PVDIS (15) and PREX (17) experiments both used the same apparatus, the JLab–Hall A high-resolution spectrometers (HRS) (18). The HRS was designed not for PVES but rather to measure cross sections with excellent

energy resolution. For that purpose, the HRS spectrometers were instrumented with a detector package with drift chambers for tracking, Cherenkov counters and an electron calorimeter made of Pb glass for particle identification.

For PREX, the spectrometers needed sufficient energy resolution to reject inelastically scattered electrons that had lost more than a few MeV. The HRS detector package was not used, but rather elastic events were focussed onto a small quartz bar and the signal was integrated. The drift chambers in the spectrometers were used in special calibration runs to measure the average Q^2 of the events giving signals in the quartz.

For PVDIS, by contrast, energy resolution was irrelevant. However, Cherenkov and Pb Glass detectors were used to identify the DIS electrons, separating them from the more copious pions. Since the electrons were identified by a coincidence between two detectors, the events must be counted.

Many PVES experiments are built around magnets originally designed for a different purpose. E122 (1), MOLLER (14), Bates (19), SoLID (20), and P2 (21) are examples. Another variation are experiments like A4 (22) and SAMPLE (23), where there is no magnet but special detectors are designed that can detect the elastic events amidst a large background of lower energy particles.

2.2.1 SPECTROMETERS: The optimization of PVES experiments is as follows. The differential cross sections and PV asymmetries are approximately,

$$\frac{d\sigma}{d\Omega} \approx \frac{E^2[FF]^2}{Q^4}, \quad A_{LR} = A_0 Q^2, \quad (11)$$

where A_0 is typically 10^{-4} to 10^{-5} GeV $^{-2}$, depending on the reaction. At first glance, it may appear that higher energies are better. However, for small angles, where $\theta \approx \sin \theta$, we can show that the statistics are independent of E . The reason is that since A_{LR} depends strongly on Q^2 , the angular acceptance $\Delta\theta$

cannot be too large; typically $\Delta\theta \sim 0.2 \times \theta$. At fixed Q^2 , $\theta \sim 1/E$. Then, the solid angle $\Delta\Omega = \sin\theta\Delta\theta\Delta\phi \approx \theta\Delta\theta\Delta\phi$, and $E^2\Delta\Omega$ is approximately constant. The statistical error varies as the ratio σ/A_{LR}^2 , which is independent of Q^2 . Thus, the main criteria for designing an experiment is to maximize the acceptance $\Delta\phi$.

Toroids, such as the one used for Qweak, typically have a large $\Delta\phi \approx \pi$. For MOLLER, where there are two electrons in the final state, full ϕ coverage can be obtained with a toroid. With a solenoid, the full 2π acceptance in ϕ can be achieved (24), as is planned for the P2 experiment. The JLab HRS spectrometers have a fixed solid angle acceptance. As a consequence, they are used at the most forward angles possible where they achieve a respectable $\Delta\phi$ of about $\pi/2$.

Another important requirement on the spectrometer, especially for experiments with elastic scattering, is energy resolution, which must be good enough to reject inelastic events. For proton scattering, pion production is the first background, so the resolution must be better than 100 MeV. For nuclear targets, inelastic levels at the 5 MeV levels must be rejected. Often a low beam energy is optimal because the rate is independent of energy but the absolute resolution improves with lower energies. By contrast, for the JLab HRS spectrometers with their excellent energy resolution, backgrounds can be rejected even with high energies and rates go up with energy due to the fixed solid angles of the HRS system.

2.2.2 DETECTORS: One important decision that influences both the design of the spectrometer and the detectors is whether to count events or to integrate the signal. Integration has the advantage that there are no pile-up or dead-time corrections. E.g., with the high resolution spectrometers in Hall A at JLab, elastically scattered events are physically separated from all inelastic events, and very clean data samples are obtained even though the signal is integrated.

For a counting experiment, the statistical error in A_{LR} is simply $1/\sqrt{N}$, where N is the number of events detected. For an integrating experiment with average signal S and detector resolution σ , the statistical error is given by,

$$\delta A_{LR} = \sqrt{\frac{1 + \sigma^2/S^2}{N}} . \quad (12)$$

Thus, if the detector has reasonable resolution, little statistics are lost by integrating. For example, for a moderate resolution $\sigma/S \sim 20\%$, the statistical error is increased by only 2%. However, care must be taken. Half of the statistics would be lost if 1% of the events has 10 times the average signal. With a thin scintillator, the Landau tail would cause σ/S to be large, and integrating the signal would cause unacceptable loss in statistics. For high energy electrons, a crude shower counter with coarse granularity will suffice. For high rates, radiation damage becomes important, and fused silica (henceforth called quartz) is the material of choice. For energies of 1 GeV and below, the resolution of a granular detector becomes poor, and thin quartz has better performance. The design is critical. If the quartz is too thin, there are too few photoelectrons detected and σ increases. If the quartz is too thick, the electrons start to shower and create a high-signal tail, which increases σ . With great care in optimizing the collection of light, acceptable performance can be achieved.

For experiments with larger asymmetries and thus lower event rates, counting techniques are practical, taking advantage of the continuous wave nature of modern electron facilities. For SoLID, a traditional electron spectrometer with tracking, Cherenkov counter, and a calorimeter is proposed.

2.2.3 DATA ACQUISITION AND ELECTRONICS: Perhaps the most specialized aspect of PVES is the electronics. Since integration is only used for PVES, the integrating electronics is custom made. For the high rate experiments, such as

SLAC–E158, PREX, and Qweak, the problem is that the statistical noise in a given helicity window is only on the order of 100 ppm, and keeping the noise of the electronics below that level is a special challenge.

For the counting experiments, the large rate of accepted events separates PVES experiments from other experiments. Custom counting electronics were a main feature of the A4 program, the JLab PVDIS experiment, and SoLID.

2.2.4 BACKGROUNDS: Backgrounds are an important source of error. The easiest case is elastic scattering where the highest energy particles possible are the desired events, and backgrounds can be eliminated simply by achieving good resolution, as is done with the JLab–Hall A HRS spectrometers. For DIS, pions are the main background, and can be separated by the usual methods.

General electromagnetic background can be a problem, especially for toroidal spectrometers. Helicity-dependence of the beam width, or other higher-order parameters which are very difficult to monitor, can propagate to the background if it arises from beam spraying from a small collimator. There can be physics asymmetries in some backgrounds, such as decay products from hyperons or pions produced by DIS events. Detailed studies are required to untangle these effects

2.3 Precision of PVES Experiments

As the field of PVES has developed, the precision achieved or proposed, both in terms of the absolute size of the error and of the fractional error in the asymmetry, has improved dramatically, as shown in **Table 2**. Most of the techniques that have been perfected over the years are common to all PVES experiments.

2.3.1 MEASURING SMALL ASYMMETRIES: The basic technique used to observe the small asymmetries in PVES is the ability to rapidly reverse the helicity

Table 2: Results from selected PV experiments. Asymmetries are given in ppm.

Experiment	Reference	Year	$-A_{LR}$	δA (stat)	δA (syst)	$\delta A/A(\%)$
SLAC-E122	(2)	1978	-120	7	6	8
Mainz	(25)	1989	-9.4	1.8	0.5	20
MIT-Bates	(19)	1990	1.62	0.37	0.11	24
SAMPLE	(23)	1990	-5.61	0.67	0.88	20
HAPPEX	(26)	2001	-15.05	0.98	0.56	7.5
GØ	(27)	2005	-2	0.15	0.2	13
Mainz-A4	(22)	2009	-17.2	0.8	0.9	5
SLAC-E158	(13)	2005	-0.131	0.014	0.010	13
HAPPEX-He	(28)	2007	6.40	0.23	0.12	4.1
PREX	(17)	2012	0.656	0.060	0.014	9.4
PREX-II		2016	(0.51)	0.015	0.005	3
CREX		2017	2.0	0.04	0.02	2.4
JLab-Hall A	(15)	2014	-160	6.4	3.1	4.4
Qweak	(10)	2013	-0.280	0.035	0.031	17
MOLLER		2020	0.035	0.0007	0.0004	2.3
SoLID	(20)	2022	-800	2	4	0.6
Mainz-P2	(21)	2018	-0.020	0.00025	0.00019	1.7
Mainz-C		2020	0.8	0.0025	0.00017	0.3

of the beam without changing any of its other properties, including energy, intensity, position, and angle. Many systematic errors that are important for measurements of cross sections, such as target thickness, spectrometer solid angle, etc.,

which are hard to measure and tend to drift with time, cancel in the asymmetry.

The source of the polarized electrons in PVES is photo-emission from a crystal, and the helicity of the beam is reversed by reversing that of the laser light producing the photo-electrons. Today, polarizations of more than 85% and beam currents of more than 100 μA are now routinely achieved by using a strained GaAsP crystal (29,30).

The helicity of the electron beam is determined by that of the laser light producing the photo-emission. The helicity of the light is reversed by using a device called a Pockels cell, which is a crystal whose birefringence is controlled by high voltage applied across the cell. To first order, the helicity is the only beam property changed by the voltage on the Pockels cell.

The improvement in the achievable precision in PVES is in part due to great progress in understanding and correcting the imperfections in the helicity reversals. The basic problem is that the laser light is partially linearly polarized, and the linear polarization also reverses with helicity. Flipping the linear component of the light causes systematic differences in the intensity, position and width of the photo-emitted electrons, the latter effects arising from a spatial dependence of the linear polarization. Extensive studies of these effects resulted in specialized techniques that have greatly improved the ability to provide clean helicity reversals.

Systematic errors can further be reduced by using independent means to reverse the beam helicity. These include insertion of a half wave plate in the laser beam, using a Wien filter in the electron beam before it is accelerated, and sometimes by running the experiment at a nearby energy where the helicity is reversed by an extra $g - 2$ flip in the accelerator or beam transport. The half-wave plate

reversals can be done every few hours; the other reversal methods are done less frequently because the accelerator needs to be retuned after the reversal.

The spectrometers in PVES experiments are designed so that they are as insensitive as possible to the beam parameters. By making the apparatus symmetrical, the signal is very insensitive to differences in beam position and angle. Careful design of apertures can reduce the sensitivity to beam size. In addition, careful tuning of the accelerator reduces the size of the helicity-correlated beam differences at the target.

Systematic differences in the beam parameters are controlled by a set of position-sensitive monitors that together determine the beam position and angle on target. A position monitor in a point of high dispersion determines energy differences in the beam. The sensitivity of the spectrometer to these beam parameters can be measured by dithering the beam with coils and an RF cavity so corrections can be made for any residual beam differences (31). Feedback is another tool, especially useful for eliminating the helicity-dependence of the beam intensity.

2.3.2 SCALE ERRORS: Although the asymmetries measured in PVES experiments are small, in many cases the fractional error $\delta A_{LR}/A_{LR}$ is on the order of 5% and the SoLID experiment proposes to measure $\delta A_{LR}/A_{LR}$ to 0.5%, which is a higher precision than most cross section experiments. Systematic errors in scale factors, such as the beam polarization P_e and Q^2 , become important.

There are two methods for measuring P_e , each with variations. One is Compton scattering from a polarized laser beam. Either the scattered electron or photon can be detected; indeed both can be detected to provide independent measurements. Theoretical errors for Compton scattering are small, and the beam polarization can be measured simultaneously with A_{LR} . Precisions as good as 1%

have been achieved and an additional factor of two is possible.

The other method is Møller scattering from a target with polarized electrons. For a ferromagnetic material in a low magnetic field, errors in the target polarization are on the order of 3%. By saturating the target in a 4 T field, this error can be reduced to below 1%. Unfortunately, the targets are thick and can tolerate currents on the order of a few μA and the polarimetry cannot be done while A_{LR} is measured. A proposed variation (32), which uses cold H atoms in a magnetic trap, features a thin target that can be run during the A_{LR} measurement, and promises to provide precision below 0.5%

3 THEORETICAL ISSUES

3.1 Effective Couplings

In an effective field theory one absorbs the effects of the heavy degrees of freedom, such as the W , the Z , and the Higgs boson mediating the weak interaction, into effective couplings. The degrees of freedom of the effective theory relevant to PVES are then electrons, first generation quarks, and nucleons. At the level of radiative corrections, discussed in Section 3.2, it is important to define the couplings in a process-independent manner and for an arbitrary gauge theory, so as to allow for direct comparisons and global analyses of the different types of experimental information. We use the conventions proposed in Reference (9) which aim to strike a balance between formal, practical and historical considerations.

After EW gauge symmetry breaking, the SM fermion fields ψ_f (with mass m_f) interact with the Higgs field H , the intermediate vector bosons W^\pm and Z , and

the photon field A , according to the Lagrangian

$$\mathcal{L} = - \sum_f \frac{m_f}{v} \bar{\psi}_f \psi_f H - \frac{g}{\sqrt{2}} \left[J_W^{\mu\dagger} W_\mu^+ + J_W^\mu W_\mu^- + J_A^\mu A_\mu + J_Z^\mu Z_\mu \right], \quad (13)$$

where v is the vacuum expectation value of H . We have chosen a common normalization in which the charged (CC), electromagnetic (EM) and weak neutral currents (NC) are given by,

$$J_W^\mu = \bar{d}_L \gamma^\mu V_{\text{CKM}}^\dagger u_L + \bar{e}_L \gamma^\mu \nu_L, \quad (14)$$

$$J_A^\mu = \sqrt{2} \sin \theta_W (Q_u \bar{u} \gamma^\mu u + Q_d \bar{d} \gamma^\mu d + Q_e \bar{e} \gamma^\mu e), \quad (15)$$

$$J_Z^\mu = \sum_f \bar{\psi}_f \gamma^\mu \left[g_L^f P_L + g_R^f P_R \right] \psi_f = \sum_f \bar{\psi}_f \gamma^\mu \frac{g_V^f - g_A^f \gamma^5}{2} \psi_f = \quad (16)$$

$$\frac{1}{\sqrt{2} \cos \theta_W} (\bar{u}_L \gamma^\mu u_L - \bar{d}_L \gamma^\mu d_L + \bar{\nu}_L \gamma^\mu \nu_L - \bar{e}_L \gamma^\mu e_L) - \tan \theta_W J_A^\mu. \quad (17)$$

Here, $\psi_{L,R} \equiv P_{L,R} \psi$ denote chiral projections, J_W^μ contains the quark mixing matrix V_{CKM} , θ_W is the weak mixing angle, and fermion generation indices have been ignored. Furthermore,

$$g_V^f \equiv g_L^f + g_R^f = \sqrt{2} \frac{T_f^3 - 2 \sin^2 \theta_W Q_f}{\cos \theta_W}, \quad g_A^f \equiv g_L^f - g_R^f = \sqrt{2} \frac{T_f^3}{\cos \theta_W}, \quad (18)$$

are vector and axial-vector Z couplings with $T_u^3 = T_\nu^3 = -T_d^3 = -T_e^3 = 1/2$.

At low energies, $Q^2 \equiv -q^2 \ll M_{W,Z}^2$, one finds the effective four-fermion interaction Lagrangians,

$$\mathcal{L}_{\text{CC}} = -\frac{2}{v^2} J_W^{\mu\dagger} J_{W\mu}, \quad \mathcal{L}_{\text{NC}} = -\frac{\cos^2 \theta_W}{v^2} J_Z^\mu J_{Z\mu}. \quad (19)$$

3.2 Radiative Corrections

The low-energy couplings defined in Equation 2 are modified by radiative corrections, which in general depend on energies, experimental cuts, etc. To render them universal, adjustments have to be applied to the underlying processes. One

defines (9) the one-loop radiatively corrected couplings to include the purely EW diagrams and certain photonic loops and γ -exchange graphs, while the remaining corrections, as e.g., the interference of two photon exchange diagrams with single γ or Z exchanges, are assumed to be applied individually for each experiment. Moreover, since the genuine EW radiative corrections will in general depend on the specific kinematical points or ranges at which the low-energy experiments are performed, one needs to introduce idealized EW coupling parameters (9) defined at the common reference scale $\mu = 0$, and expect the experimental collaborations to adjust to their conditions. According to the calculations from References (33, 34, 35, 36), the SM expressions for the NC couplings defined in this way (9) are given by,

$$g_{AV}^{\ell f} = \rho \left[-T_f^3 + 2Q_f \hat{s}_0^2 - 2Q_f \not{\varphi}_{\ell Z} + \square_{ZZ} + \square_{\gamma Z} \right] - 2Q_f \not{\varphi}_{\ell W} + \square_{WW} , \quad (20)$$

$$g_{VA}^{\ell f} = \rho \left[-T_f^3 (1 - 4\hat{s}_0^2) + 2\not{\varphi}_{fZ} + \square'_{ZZ} + \square'_{\gamma Z} \right] + 2\not{\varphi}_{fW} + \square_{WW} , \quad (21)$$

where using the abbreviations $\hat{\alpha}_V \equiv \hat{\alpha}(M_V)$ and $\hat{\alpha}_{ij} \equiv \hat{\alpha}(\sqrt{m_i M_j})$, one has,

$$\not{\varphi}_{fW} = \frac{\alpha}{6\pi} \left[(Q_f - 2T_f^3) \left(\ln \frac{M_W^2}{m_p^2} + \frac{1}{6} \right) - \frac{8}{3} T_f^3 \right] , \quad (22)$$

$$\not{\varphi}_{fZ} = \frac{\alpha}{6\pi} Q_f g_{VA}^{ff} \left(\ln \frac{M_Z^2}{m_f^2} + \frac{1}{6} \right) , \quad (23)$$

$$\square_{WW} = -\frac{3\hat{\alpha}_Z}{16\pi\hat{s}_Z^2} \left[1 - \frac{\hat{\alpha}_s(M_W)}{\pi} + \frac{2}{3} T_f^3 \left(5 - \frac{\hat{\alpha}_s(M_W)}{\pi} \right) \right] , \quad (24)$$

$$\square_{ZZ} = -\frac{3\hat{\alpha}_Z}{16\pi\hat{s}_Z^2\hat{c}_Z^2} \left(g_{VA}^{\ell f} g_{VV}^{\ell f} + g_{AV}^{\ell f} g_{AA}^{\ell f} \right) \left[1 - \frac{\hat{\alpha}_s(M_Z)}{\pi} \right] , \quad (25)$$

(the QCD correction needs to be dropped if f refers to a lepton) and \square'_{ZZ} is given by \square_{ZZ} with $g_{VA}^{\ell f} \leftrightarrow g_{AV}^{\ell f}$. Furthermore,

$$\square_{\gamma Z} = \frac{3\hat{\alpha}_{fZ}}{2\pi} Q_f g_{VA}^{\ell f} \left[\ln \frac{M_Z^2}{m_f^2} + \frac{3}{2} \right] , \quad \square'_{\gamma Z} = \frac{3\hat{\alpha}_{pZ}}{2\pi} Q_f g_{AV}^{\ell f} \left[\ln \frac{M_Z^2}{m_p^2} + \frac{5}{6} \right] . \quad (26)$$

Table 3: SM values of the one-loop and leading two-loop corrected effective NC couplings entering PVES for the charged SM fermions, the nucleons, and carbon, where the latter cases refer to the coherent sums over constituent quark.

f	e	u	d	p	n	$2u - d$	^{12}C
g_{AV}^{ef}	0.0225	-0.1887	0.3419	-0.0355	0.4951	-0.7192	2.7573
g_{VA}^{ef}	0.0225	-0.0351	0.0248	-0.0454	0.0144	-0.0950	-0.1859

In these relations, the parameter ρ (37) renormalizes the NC interaction strength at low energies, and \square_{WW} and \square_{ZZ} denote EW box diagrams. The logarithms entering the quark charge radii, \varnothing_{qW} and \varnothing_{qZ} , are regulated at the strong interaction scale, Λ_{QCD} , introducing a hadronic theory uncertainty into the $g_{VA}^{\ell q}$ unless they are extracted from DIS (in these expressions $m_q = m_p$ by *definition*).

Numerically most important are vacuum polarization diagrams of γ - Z mixing type giving rise to a scale-dependence (38) of the weak mixing angle. As long as one stays in the perturbative QCD domain these effects can be re-summed (39), while passing Λ_{QCD} introduces a hadronic uncertainty (see Section 3.3). At the tree level we employ the weak mixing angle at the scale $\mu = 0$ and abbreviate, $\hat{s}_0^2 \equiv \sin^2 \hat{\theta}_W(0)$, while in the EW box graphs the use of $\hat{s}_Z^2 \equiv \sin^2 \hat{\theta}_W(M_Z)$ is more suitable (the caret indicates the definition in the $\overline{\text{MS}}$ -renormalization scheme). In \varnothing_{fZ} and in the γZ box diagrams discussed in Section 3.3 we use $\mu^2 = m_f M_Z$ (9). The resulting SM values of the NC couplings are given in **Table 3**.

Unlike the quantities C_{1q} and C_{2q} defined (33) in the context of APV we exclude the small axial current QED renormalization factors $(1 - Q_f^2 \alpha / 2\pi)$ from the definitions of g_{AV}^{ef} and g_{VA}^{ef} , because QED and QCD corrections to external lines are not considered part of the EW couplings. They can be included together

with experiment specific initial and final state radiation effects and $\gamma\gamma$ box graphs in explicit QED radiative correction factors (40) multiplying the asymmetries. In addition, $\not{e}Z$ and the γZ box contributions need to be adjusted for $Q^2 \neq 0$, which in the case of Møller scattering amounts to shifts (9)

$$g_{VA}^{ee} \rightarrow g_{VA}^{ee} + 0.0010 \pm 0.0004 , \quad g_{VA}^{ee} \rightarrow g_{VA}^{ee} + 0.0008 \pm 0.0005 , \quad (27)$$

for the SLAC (13) and Jefferson Lab (14) experiments, respectively.

In the DIS regime, the γZ box graphs need to be adjusted for the relevant Q^2 -values and beam energies, but this is feasible (41) and the extra Q^2 -dependences are expected to change the A_{LR}^{DIS} by at most a few ‰. Ignoring this issue, the adjustments for the SLAC (2) and Jefferson Lab (15, 42) experiments, all with Q^2 -values around the charm quark threshold, are

$$g_{AV}^{eq} \rightarrow g_{AV}^{eq} - 0.0011 Q_q \ln \frac{Q^2}{0.14 \text{ GeV}^2} . \quad (28)$$

$$g_{VA}^{eu} \rightarrow g_{VA}^{eu} - 0.0009 \ln \frac{Q^2}{0.078 \text{ GeV}^2} , \quad (29)$$

$$g_{VA}^{ed} \rightarrow g_{VA}^{ed} + 0.0007 \ln \frac{Q^2}{0.021 \text{ GeV}^2} . \quad (30)$$

The most precise current constraints on the corrected $g_{AV}^{en} \equiv g_{AV}^{eu} + 2g_{AV}^{ed}$ and $2g_{AV}^{eu} - g_{AV}^{ed}$ as functions of $2g_{VA}^{eu} - g_{VA}^{ed}$ are shown in **Figure 1**.

3.3 Theoretical Uncertainties

The corrections that need to be applied in order to extract the coefficients g_{AV}^{ef} and g_{VA}^{ef} introduce additional uncertainties. These are relatively enhanced whenever the tree-level expression is suppressed by a factor $1 - 4\hat{s}_0^2 \approx 0.045$, as is the case for all the g_{VA}^{ef} , as well as the g_{AV}^{ef} for the electron and the proton. The most important associated theoretical uncertainties are from the renormalization group

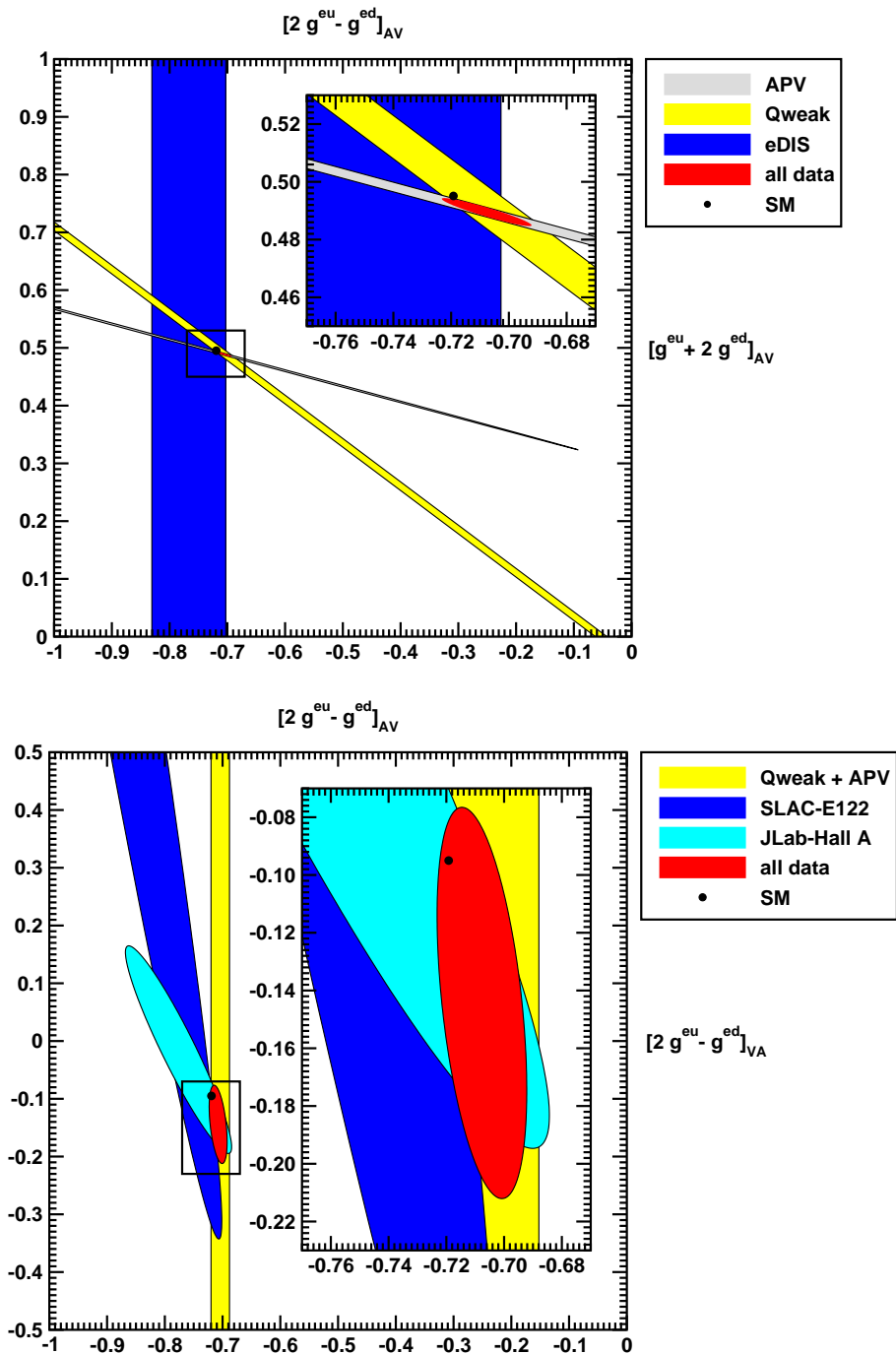


Figure 1: Experimentally determined coupling combinations g_{AV}^{en} (upper plot) and $2g_{VA}^{eu} - g_{VA}^{ed}$ (lower plot) vs. $2g_{AV}^{eu} - g_{AV}^{ed}$ compared to the SM prediction. The APV constraint is from Cs and Tl and forms a strongly elongated ellipse rather than a band.

evolution (running) of the weak mixing angle (38,39) and γZ -box diagrams (both involving hadronic effects), as well as from unknown higher order EW corrections.

3.3.1 $\sin^2 \hat{\theta}_W(0)$: The running of $\sin^2 \hat{\theta}_W$ from $\mu = M_Z$ (where it has been measured precisely in Z -pole experiments) to $\mu = 0$ arises from loop-induced γ - Z mixing diagrams and amounts to a 3.2% effect. There is currently a relative 0.9% theoretical uncertainty in its calculation (39) which translates to a 0.6% uncertainty in the Møller asymmetry and a 0.4% uncertainty for the ep asymmetry (it would be a negligible 0.03% for measurements in carbon).

Most of the scale evolution ($\sim 75\%$) can be computed reliably within perturbation theory, but the contribution below m_c requires other considerations. In this regime one can estimate the effect by relating it to that of the EM coupling, $\hat{\alpha}(\mu)$ (43), which in turn is determined by computing a dispersion integral over e^+e^- cross-section data and (up to isospin breaking effects) to τ decay spectral functions (44). The corresponding error contribution is about $\pm 3 \times 10^{-5}$ in \hat{s}_0^2 and fully correlated with the one in $\hat{\alpha}$.

This strategy is limited by the necessary separation of the contributions from the various quark flavors and from QCD annihilation (or singlet) diagrams which enter $\hat{\alpha}$ and $\sin^2 \hat{\theta}_W$ differently. The largest uncertainty (5×10^{-5}) is induced by the need to quantify the strange quark contribution relative to the first generation quarks. In the future it may be possible to decrease this error by including information about the strange meson production fraction, but this is complicated due to the occurrence of secondary strange pair production. Isospin breaking due to $m_u \neq m_d$ contributes an additional but much smaller ($\sim 10^{-5}$) uncertainty. Currently an error of 3×10^{-5} is assigned to the singlet separation (39), but since QCD annihilation diagrams are related to Okubo-Zweig-Iizuka (OZI) rule

violations which are phenomenologically known to be strongly suppressed, this is quite likely an overestimate.

In addition, there are parametric uncertainties from the imperfect knowledge of α_s , m_b and m_c . They could increase the above error estimates by up to 30%, but it can be expected that they will be much better determined in the future, e.g., by means of lattice simulations. In any case, these are fundamental fit parameters allowed to vary in EW fits, and should not be added to the purely theoretical uncertainties reviewed here.

3.3.2 HADRONIC γZ BOX: From Equation 26 one can see that the contributions from γZ box diagrams are logarithmically enhanced. Moreover, and more importantly, these logarithms are sometimes regulated at the scale Λ_{QCD} (we chose the reference value m_p while the full effect depends on experimental and kinematical details). This signals a hadronic uncertainty and is indicated when the parton model expression introduces the logarithm of the mass of a quark. Fortunately, the sum of uncrossed and crossed γZ box diagrams entering APV gives rise to the chiral structure $\square_{\gamma Z}$ which is itself suppressed by $1 - 4\hat{s}_0^2$. This is the reason why this kind of uncertainty is small in APV (34, 45).

The finite beam energy, E_e , in PVES, on the other hand, upsets the cancellation between uncrossed and crossed γZ box graphs, effectively introducing the wrong-chirality and unsuppressed structure $\square'_{\gamma Z}$ (46). Several groups estimated the effect and there is consensus regarding the central value. The most recent evaluation (47) of the sum of the two chiral structures applicable to the Qweak condition with $E_e = 1.165$ GeV implies the correction,

$$g_{AV}^{ep} \rightarrow g_{AV}^{ep} - 0.0027 \pm 0.0007 \text{ (CEBAF)} . \quad (31)$$

The uncertainty is dominated by the $\square'_{\gamma Z}$ structure and, respectively, smaller

and larger by more than a factor of two compared to the ones quoted in (48) and (49). A reduction and robust estimate of the error will be important for a solid interpretation of the Qweak experiment (50). Further hadronic effects of relative order Q^2 and their uncertainties ($\approx 1.5\%$) are treated by extrapolating the Qweak and other PVES data points to $Q^2 = 0$, as e.g., in Reference (51). The γZ box corrections, uncertainties, and correlations need to be applied to each data point in the extrapolation.

The beam energy of MESA for the P2 project is still subject to optimizations, but it will be low enough that the $\square_{\gamma Z}$ uncertainty dominates. For $E_e = 200$ MeV, the analysis of Reference (47) implies the correction,

$$g_{AV}^{ep} \rightarrow g_{AV}^{ep} - 0.0008 \pm 0.0003 \text{ (MESA)} . \quad (32)$$

Effects due to $Q^2 \neq 0$ in the shifts 31 and 32 are negligible (48), and the Q^2 -dependence of the weak mixing angle can be ignored if the asymmetry is normalized using the fine structure constant in the Thomson limit. But the electron charge radius induces the additional shift (9),

$$g_{AV}^{ep} \rightarrow g_{AV}^{ep} - 0.00008 \ln \frac{Q^2}{0.00021 \text{ GeV}^2} . \quad (33)$$

In the DIS regime, the γZ box can be calculated perturbatively, but the appropriate event generators (52) need to be examined for consistency with more recent conventions and refinements. This will introduce an additional Q^2 -extrapolation.

3.3.3 UNKNOWN HIGHER ORDERS: Several EW one-loop corrections are large, most notably the WW box contribution to the ep asymmetry which exceeds the anticipated experimental precision by an order of magnitude. Thus, the α_s terms (36) in Equations 24 and 25, as well as other higher order effects need to be included or induce additional uncertainties. For example, the uncertainties

displayed in Equation 27 arise from scale uncertainties in one-loop terms. Some reducible contributions can be determined by renormalization group and similar techniques, but a full two-loop calculation (ideally including enhanced three-loop effects) appears feasible and should be vigorously pursued (53).

4 HADRONIC STRUCTURE

The idealized form of the DIS asymmetry for a deuteron target in Equation (10), is modified by various hadronic corrections to

$$A_{LR}^{\text{DIS}} = -\frac{3}{20\pi\alpha} \frac{Q^2}{v^2} \left[\tilde{a}_1 + \tilde{a}_2 \frac{1 - (1 - y)^2}{1 + (1 - y)^2} \right], \quad (34)$$

where the parameters \tilde{a}_j ($j = 1, 2$) have the form

$$\tilde{a}_j = (2g_j^{eu} - g_j^{ed}) [1 + R_j(\text{sea}) + R_j(\text{CSV}) + R_j(\text{TM}) + R_j(\text{HT})], \quad (35)$$

and where $g_1^{eq} \equiv g_{AV}^{eq}$ and $g_2^{eq} \equiv g_{VA}^{eq}$. The quantities $R_j(\text{sea})$, $R_j(\text{CSV})$, $R_j(\text{TM})$ and $R_j(\text{HT})$ denote corrections arising from sea-quarks, charge symmetry violation, target mass effects, and higher twist effects, respectively. Below we discuss some of these hadronic effects and their potential impact on the theoretical interpretation of precision PVDIS measurements.

Within the SM, it is often convenient to write Equation 34 in terms of the five EW structure functions $F_{1,2}^\gamma$ and $F_{1,2,3}^{\gamma Z}$ as

$$A_{LR}^{\text{DIS}} = \frac{1}{8\pi\alpha} \frac{Q^2}{v^2} \left[Y_1 \frac{F_1^{\gamma Z}}{F_1^\gamma} + \frac{Y_3}{2} \frac{F_3^{\gamma Z}}{F_1^\gamma} \right]. \quad (36)$$

Note, that deviating from common conventions, we have absorbed g_A^e and g_V^e , in the first and second term, respectively, into the structure function. The functions

Y_1 and Y_3 functions have the form

$$Y_1 = \left[\frac{1 + R^{\gamma Z}}{1 + R^\gamma} \right] \frac{1 + (1 - y)^2 - y^2 \left[1 - \frac{r^2}{1 + R^{\gamma Z}} \right] - 2xy \frac{M}{E}}{1 + (1 - y)^2 - y^2 \left[1 - \frac{r^2}{1 + R^\gamma} \right] - 2xy \frac{M}{E}},$$

$$Y_3 = \left[\frac{r^2}{1 + R^\gamma} \right] \frac{1 - (1 - y)^2}{1 + (1 - y)^2 - y^2 \left[1 - \frac{r^2}{1 + R^\gamma} \right] - 2xy \frac{M}{E}}, \quad (37)$$

where R^γ and $R^{\gamma Z}$ denote the ratios of the longitudinal to transverse virtual photon cross-sections, for the EM (γ) and the interference (γZ) contributions, respectively. They are given in terms of the structure functions as

$$R^{\gamma(\gamma Z)} = r^2 \frac{F_2^{\gamma(\gamma Z)}}{2xF_1^{\gamma(\gamma Z)}} - 1, \quad r^2 \equiv 1 + \frac{4M^2x^2}{Q^2}, \quad x \equiv \frac{Q^2}{ys}. \quad (38)$$

In the (Bjorken) limit, $Q^2 \rightarrow \infty$, in which the Bjorken variable x is kept fixed, the structure functions satisfy the Callan-Gross relations, $F_2^{\gamma(\gamma Z)} = 2xF_1^{\gamma(\gamma Z)}$, and

$$Y_1 \rightarrow 1, \quad Y_3 \rightarrow \frac{1 - (1 - y)^2}{1 + (1 - y)^2}. \quad (39)$$

In this limit and ignoring sea quarks and CSV, A_{LR}^{DIS} for the isoscalar deuteron target takes the simple form in Equation (10). All structure function effects cancel, allowing for a clean extraction of the g_{AV}^{eq} and g_{VA}^{eq} coefficients.

4.1 Higher Twist Effects

The PVDIS asymmetry for electron-deuteron scattering is particularly interesting as a probe of long range quark and gluon correlations, which go beyond the leading twist (twist-2) parton model. They give rise to higher twist Q^2 -dependent power corrections encoded in $R_1(\text{HT})$ and $R_2(\text{HT})$. It was first shown in References (54, 55) that the twist-4 contribution to $R_1(\text{HT})$ is due to the deuteron (D) matrix element of a single four-quark operator,

$$W_{\mu\nu}^{du} = \frac{1}{M_D} \int \frac{d^4x}{2\pi} e^{iq \cdot x} \langle D(\vec{P}) | \frac{\bar{d}(x)\gamma_\mu d(x) \bar{u}(0)\gamma_\nu u(0) + (u \leftrightarrow d)}{2} | D(\vec{P}) \rangle. \quad (40)$$

$R_2(\text{HT})$, which receives contributions from several twist-4 operators, is relatively suppressed by g_{VA}^{eq} and can be isolated from $R_1(\text{HT})$ through its y -dependence. It was also shown in References (54,55) that $R_2(\text{HT})$ is related to the higher twist effects appearing in neutrino-deuteron charged-current DIS. These properties allow for a relatively clean theoretical interpretation of the quark-quark correlation in Equation 40, provided that $R_1(\text{HT})$ is large enough to be observed.

Several earlier works (56, 57, 58, 59, 60, 61, 62) have explored various aspects of HT effects in PVDIS. More recently (63, 64), the HT phenomenology was revisited in the context of the current generation of high precision experiments. In the form of A_{LR}^{DIS} given in Equation 36, the Y_1 term can receive contributions from HT effects if $R^{\gamma Z} \neq R^\gamma$ and from the ratio $F_1^{\gamma Z}/F_1^\gamma$. In the absence of empirical data on $R^{\gamma Z}$, the impact of $R^{\gamma Z} \neq R^\gamma$ was explored in Reference (63) and it was found that the variation $R^{\gamma Z} = R^\gamma \pm 10\%$ resulted in a $\sim 0.5\%$ shift in A_{LR}^{DIS} . In subsequent work (64), the Bjorken-Wolfenstein (54, 55) argument was applied to the Y_1 term and it was shown that the equality $R^{\gamma Z} = R^\gamma$ was true even at twist-4 up to perturbative corrections — a consequence of the twist-4 structure functions associated with $W_{\mu\nu}^{du}$ satisfying the tree-level Callan-Gross relation $F_2^{du} = 2xF_1^{du}$ (65,66,67). Instead, the dominant HT effects arises through the ratio $F_1^{\gamma Z}/F_1^\gamma$, giving rise to the correction

$$R_1(\text{HT}) = \frac{-4}{5 \left(1 - \frac{20}{9} \sin^2 \theta_W\right)} \frac{F_1^{du}}{u_p(x) + d_p(x)}, \quad (41)$$

where u_p (d_p) is the u (d) quark parton distribution function (PDF) in the proton.

The first estimates of the twist-4 contribution to $R_1(\text{HT})$ were obtained (56,57) within the MIT Bag Model (68) by rescaling the twist-2 contribution by the ratio of their leading moments. This computation was recently (64) extended to include the effects of higher spin operators. A model for the nucleon wave functions in the

light-cone formalism (69,70,71) was used to obtain an independent estimate (72) for $R_1(\text{HT})$. Most recently (73), quark orbital angular momentum dynamics was added and its effect on $R_1(\text{HT})$ was studied. It was found that $R_1(\text{HT})$ was largely insensitive to quark angular momentum due to cancellations between its different components. All of these recent studies yield similar results in the range $R_1(\text{HT}) \sim 0.002$ to 0.005 in the valence region of x . This is likely too small to be measured by SoLID which is expected to measure A_{LR}^{DIS} to $\sim 0.5\%$ precision, and indicates that A_{LR}^{DIS} can probe CSV or new physics without HT contamination. On the other hand, if a large Q^2 -dependent effect is observed in the Y_1 -term, it would be a clear indication of interesting long range quark-quark correlations that are not adequately described by current theoretical models.

4.2 Charge Symmetry Violation

Most early phenomenological work on PDF assumed charge symmetry, meaning that the u (d) quark PDF in the proton was set equal to the d (u) quark PDF in the neutron

$$u_p(x) = d_n(x) , \quad d_p(x) = u_n(x) . \quad (42)$$

CSV is expected to arise from quark mass differences and the effects of QED splitting functions (74, 75, 76) on the DGLAP evolution of PDF. Several non-perturbative models (77, 78, 79) of the nucleon have been studied to estimate the size of CSV effects. While no conclusive evidence of CSV has been observed, it is constrained from an analysis of high energy data (74). The strongest limit on CSV arises from comparison of the F_2 structure functions between charged lepton DIS and neutrino charged current DIS on isoscalar nuclear targets. For a recent detailed review on CSV and experimental constraints, we refer the reader

to Reference (80).

The CSV effects can be parameterized in terms of the quantities δu and δd ,

$$\delta u(x) \equiv u_p(x) - d_n(x) , \quad \delta d(x) \equiv d_p(x) - u_n(x) . \quad (43)$$

Then, the CSV corrections to A_{LR}^{DIS} in Equations 34 and 35 take the form,

$$R_i(\text{CSV}) = \left[\frac{1}{2} \left(\frac{2g_i^{eu} + g_i^{ed}}{2g_i^{eu} - g_i^{ed}} \right) - \frac{3}{10} \right] \left(\frac{\delta u - \delta d}{u + d} \right) . \quad (44)$$

A global fit to high energy data was performed by the MRST group (74) using the phenomenological form,

$$\delta u - \delta d = 2\kappa x^{-1/2}(1-x)^4(x-0.0909) , \quad (45)$$

that yielded a best fit value of $\kappa = -0.2$ and a 90% confidence interval given by $-0.8 \leq \kappa \leq 0.65$. In **Figure 2**, we show the CSV correction $R_1(\text{CSV})$ for the end points of this interval. For comparison we also show the MIT Bag model estimate (64) of the HT correction $R_1(\text{HT})$. This estimate for $R_1(\text{HT})$, similar in size to other estimates (56, 57, 72, 73), indicates that the Y_1 -term of A_{LR}^{DIS} can probe percent level CSV effects, without much contamination from HT effects. The CSV effects on the total asymmetry, including both $R_1(\text{CSV})$ and $R_2(\text{CSV})$, are also at the percent level (63) of the 90% confidence interval, which should be contrasted with the expected precision of SOLID at the 0.5% level.

Flavor-dependent effects can also arise for PDF in heavier nuclei through isospin-dependent nuclear forces affecting the u - and d quark distributions differently. Several works (81, 82, 83, 84, 85, 86, 87) have been devoted to understanding the underlying mechanisms responsible for differences in the cross sections per nucleon among various nuclei. Recently, nuclear-dependent effects were also studied (88) using a newly introduced (89, 88, 90, 91) DIS event shape called 1-jettiness (92). Differences in the PDF in the valence region of x , due to nuclear

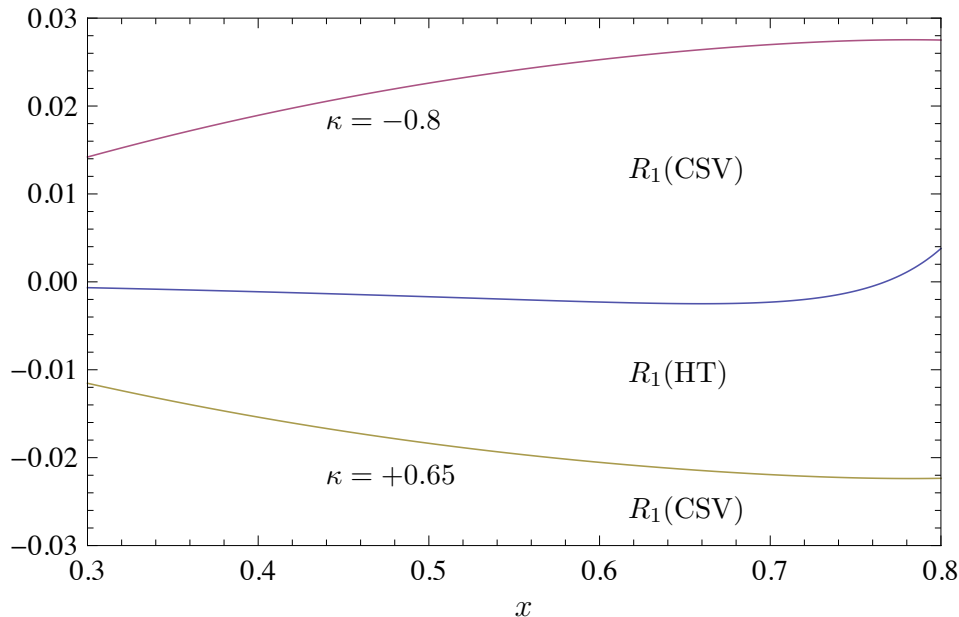


Figure 2: The relative magnitudes of $R_1(\text{HT})$ and $R_1(\text{CSV})$ as a function of x for a representative value of $Q^2 = 6 \text{ GeV}^2$. The top and bottom curves give $R_1(\text{CSV})$ for the choices $\kappa = -0.8$ and $\kappa = 0.65$, respectively, using Equations 44 and 45. The middle curve (64) is the MIT Bag Model estimate for $R_1(\text{HT})$. Figure reprinted from Reference (64).

effects, are referred to as the EMC (93) effect. An unambiguous picture of the mechanisms responsible for the EMC effect is still lacking after more than two decades of investigation.

Recently, PVDIS on nuclei has been proposed (94) as a novel probe of the flavor dependence of the nuclear EMC effect, which appears dominantly as an isovector correction to the \tilde{a}_1 term in Equation 34,

$$\delta\tilde{a}_1(x_A) \simeq -\frac{12}{25} \frac{u_A^+(x_A) - d_A^+(x)}{u_A^+(x_A) + d_A^+(x)}, \quad (46)$$

where x_A is the parton momentum fraction in the nucleus multiplied by the atomic weight A and $q_A^+(x_A) \equiv q_A(x_A) + \bar{q}_A(x_A)$. For isoscalar targets, ignoring heavy quark flavors, quark mass differences, and EW corrections, this correction

vanishes since the u and d quark nuclear distributions u_A and d_A are identical. However, for other nuclear targets with $N \neq Z$, this isovector EMC correction could be large. Such a PVDIS analysis on an iron or lead target could provide insight into the impact of this EMC effect on the extraction of the weak mixing angle at NuTeV (93). In general, combining $\delta\tilde{a}_1(x_A)$ from PVDIS analyses with data on EM DIS, may allow to extract flavor-dependent nuclear PDF.

4.3 Extracting the d/u Ratio of Parton Distribution Functions

A measurement of A_{LR}^{DIS} on a proton target is sensitive (95) to the ratio of the d to u quark PDF. The standard determination of the d/u ratio relies on fully inclusive DIS on a proton target compared to a deuteron target. In the large x region, nuclear corrections in the deuteron target lead to large uncertainties in the d/u ratio. Several methods (96, 97, 98, 99, 100, 101) to control these nuclear uncertainties have been investigated. However, they can be completely eliminated if the d/u ratio is obtained from the proton target alone. For this reason, precision measurements of A_{LR}^{DIS} on a proton target can be a powerful probe of the d/u ratio.

A_{LR}^{DIS} in Equation 36 for a proton target at leading twist takes the form,

$$A_{LR}^p = -\frac{1}{4\pi\alpha} \frac{Q^2}{v^2} [Y_1 a_1^p + Y_3 a_2^p] , \quad (47)$$

where the coefficients a_1^p and a_2^p depend on the d/u ratio,

$$a_1^p = \frac{12 g_{AV}^{eu} - 6 g_{AV}^{ed} d/u}{4 + d/u} , \quad a_2^p = \frac{12 g_{VA}^{eu} - 6 g_{VA}^{ed} d/u}{4 + d/u} . \quad (48)$$

As in the case of the deuteron asymmetry, other hadronic corrections can affect the extraction of the d/u ratio. Reference (63) performed an analysis of finite- Q^2 effects in the Y_1 and Y_3 factors and studied their impact on the extraction of d/u . For finite- Q^2 effects arising from $r \neq 1$ and $R^\gamma \neq 0$, where the parameterization

in Reference (102) was used for R^γ , a shift in A_{LR}^{DIS} in the 1 to 2% range was found at $Q^2 = 5 \text{ GeV}^2$ and for $0.6 \lesssim x \lesssim 0.8$, with an uncertainty of $\pm 0.5\%$. This shift increased to about 3% for $x \simeq 0.9$ with an uncertainty of $\pm 1\%$. Another hadronic effect arises from possible differences between R^γ and $R^{\gamma Z}$. It was found (63) that a 10% (20%) difference led to a 1% (2%) shift in A_{LR}^{DIS} . Both finite- Q^2 effects are to be compared with shifts in the 3 to 10% range arising from different possible behaviors (103, 104, 105) of the d/u ratio at large x . This analysis indicates that precision measurements of PVDIS on a proton target could provide useful information on the d/u ratio in the region of large x .

5 NUCLEAR PHYSICS

PVES can map the distribution of weak charge in a nucleus. This provides largely model independent neutron densities because the weak charge of a neutron is much larger than that of a proton. In this section we discuss the PREX and PREX II experiments on ^{208}Pb and the approved CREX experiment on ^{48}Ca . We conclude this section commenting on a precision measurement of the weak charge of ^{12}C from electron scattering at low Q^2 . This would involve precision comparable to or better than the approximately 0.3% APV measurement of the weak charge of Cs. One would need high statistics, small systematic errors and accurate normalization, including high accuracy measurements of beam polarization. However, if this could be achieved the resulting determination of the weak charge of ^{12}C would be free from atomic structure uncertainties that may complicate the interpretation of APV.

The formalism is presented in Section 5.1, while Section 5.2 relates the atomic PV asymmetry to the thickness of the expected neutron rich skin and to the

density dependence of the symmetry energy. This important nuclear structure quantity describes how the energy of nuclear matter increases as one goes away from equal numbers of neutrons and protons. Section 5.3 discusses important applications to astrophysics for inferring the pressure of neutron matter and the structure of neutron stars. Finally, in Section 5.4 we briefly discuss the experiments on ^{208}Pb (PREX and PREX II), ^{48}Ca (CREX), and ^{12}C .

5.1 Nuclear Formalism

In this section we calculate the weak charge density of a heavy nucleus and the PV asymmetry A_{LR} . For simplicity we consider spin zero nuclei. We start by defining the weak charges of the proton Q_p and neutron Q_n as minus twice the corresponding coupling constants of **Table 3**. We use $Q_p = -2g_{AV}^{ep} = 0.0710$ and $Q_n = -2g_{AV}^{en} = -0.9902$, and recall that Q_p is small, includes important radiative corrections, and is being measured by the Qweak experiment (10). In contrast, Q_n is large, includes modest radiative corrections, and is constrained by Cs APV. We reiterate (see Section 3.2) that at the level of small radiative corrections these definitions of Q_p and Q_n differ from the standard convention (33).

The weak charge density of a heavy nucleus,

$$\rho_W(r) = \int d^3r' [4G_n^Z(|\mathbf{r} - \mathbf{r}'|)\rho_n(r') + 4G_p^Z(|\mathbf{r} - \mathbf{r}'|)\rho_p(r')] , \quad (49)$$

is modeled as point proton and neutron densities, ρ_p and ρ_n , folded with appropriate single nucleon weak form factors. The densities ρ_p and ρ_n are normalized to the proton, $Z = \int d^3r \rho_p(r)$, and neutron, $N = \int d^3r \rho_n(r)$, numbers of the nucleus. This neglects possible meson exchange currents that are expected to be small because mesons likely transport weak charge only over distances small compared to the nuclear weak radius (106). However, see also the spin-orbit

contributions to weak charge densities discussed in (107).

The weak single nucleon form factors of the proton, G_p^Z , and neutron, G_n^Z , Fourier transformed into coordinate space, are

$$4G_p^Z = Q_p G_E^p + Q_n G_E^n - G_E^s , \quad (50)$$

$$4G_n^Z = Q_n G_E^p + Q_p G_E^n - G_E^s . \quad (51)$$

Here the (EM) Electric form factor of the proton is G_E^p and the Electric form factor of the neutron is G_E^n . Finally, strange quark contributions to the Electric form factor, G_E^s , are constrained by several previous measurements and will be neglected in the following. The weak form factor $F_W(Q^2)$ is defined,

$$F_W(Q^2) = \frac{1}{Q_W} \int d^3r j_0(Qr) \rho_W(r) , \quad (52)$$

where j_0 is a spherical Bessel function. The total nuclear weak charge is given by

$$Q_W = \int d^3r \rho_W(r) = NQ_n + ZQ_p . \quad (53)$$

In the Born approximation, the PV cross-section asymmetry for longitudinally polarized electrons elastically scattered from an unpolarized nucleus, A_{LR} , is

$$A_{LR} \approx \frac{1}{8\pi\alpha} \frac{Q^2}{v^2} \frac{Q_W}{Z} \frac{F_W(Q^2)}{F_{ch}(Q^2)} , \quad (54)$$

where $F_{ch}(Q^2)$ is the Fourier transform of the known charge density and is normalized so that $F_{ch}(Q^2 = 0) = 1$.

For a heavy nucleus, the Born approximation is not adequate and there are important corrections from Coulomb distortions that are of order $Z\alpha$. It is useful to distinguish Coulomb distortions, that involve the exchange of an additional photon where the nucleus remains in the same state, from dispersion corrections. Dispersion corrections involve excited intermediate states and are order α (instead

of $Z\alpha$). Comparison of ^{208}Pb cross section measurements with positrons and electrons suggest that dispersion corrections are small (108).

Coulomb distortions can be accurately calculated by solving the Dirac equation for an electron moving in both a Coulomb potential, that is of order 25 MeV for ^{208}Pb , and an axial vector potential of order $G_F\rho_W \approx 10$ eV (109). The cross section for positive helicity involves an electron scattering in the sum of axial and vector potentials, while the cross section for negative helicity involves scattering from the difference of the vector minus the axial potentials. These Coulomb distortion calculations are good to all orders in $Z\alpha$ and involve little uncertainty because the charge density is accurately known.

5.2 Neutron Skins and the Symmetry Energy

PVES can determine the neutron skin thickness, $\Delta R = R_n - R_p$, defined as the difference between the root mean square (point) neutron radius, R_n , and the proton radius, R_p . Note that R_p is often known from measured charge radii. Theoretical predictions for ΔR , for nuclei all across the periodic table, are discussed in Reference (110). The skin thickness is determined largely by isovector parts of nuclear interactions that are, in general, not well constrained by fitting binding energies and charge radii of conventional nuclei.

Instead, the skin thickness is closely related to the density dependence of the symmetry energy. The energy per particle of asymmetric matter, $\rho_n \neq \rho_p$, is

$$\frac{E}{A}(\rho_n \neq \rho_p) \approx \frac{E}{A}(\rho_n = \rho_p) + \alpha^2 S(\rho) . \quad (55)$$

Here the neutron excess is $\alpha = [(\rho_n - \rho_p)/\rho]^2$ with $\rho = \rho_n + \rho_p$. The symmetry energy $S(\rho)$ describes how the energy of nuclear matter increases as one moves away from equal numbers of neutrons and protons. It is a function of density

ρ , and arises from the Pauli exclusion principle and because nucleon-nucleon interactions are more attractive in isospin zero, compared to isospin one states.

As an example, ^{208}Pb has 44 more neutrons than protons. If these extra neutrons are placed at a density ρ in the nucleus, then there will be an energy cost $S(\rho)$. If the symmetry energy is independent of density, surface tension will push the extra neutrons to high densities and the neutron skin will be small. However, if $S(\rho)$ increases rapidly with density, the symmetry energy will favor putting the extra neutrons at low densities in the nuclear surface and this will give a large ΔR . Therefore there is a strong correlation between the neutron skin thickness in ^{208}Pb and the density dependence of the symmetry energy L (111). This parameter is defined as,

$$L = 3\rho_0 \left. \frac{dS}{d\rho} \right|_{\rho_0}, \quad (56)$$

where the nuclear saturation density is $\rho_0 = 0.16 \text{ fm}^{-3}$. There is a great deal of interest in determining L from other nuclear structure measurements and heavy ion collisions (112). Measuring ΔR with PVES likely provides the most model independent way to determine L .

5.3 Neutron Skins and Astrophysics

The neutron skin thickness is also important for astrophysics. The pressure of neutron matter is closely related to the density dependence of the symmetry energy. Typel and Brown showed that there is a strong correlation between the neutron skin thickness in ^{208}Pb , as predicted by many density functionals, and the pressure of neutron matter at a density near 0.1 fm^{-3} (113). The larger the pressure, the more neutrons are pushed out against surface tension, and the larger the neutron skin.

The structure of neutron stars is determined by the equation of state, pressure versus energy density, of neutron rich matter. The higher the pressure, the further out matter is supported against gravity and the larger the neutron star radius. Thus, in general one expects a correlation between the neutron skin thickness in ^{208}Pb and the radius of a neutron star (114,115). A thick neutron skin suggests a large pressure and a large neutron star radius.

There is great interest in X-ray observations of neutron star radii R_{NS} . If one can determine the luminosity $L_{X\text{-ray}}$ and surface temperature T , from X-ray spectra, one can infer an effective surface area $4\pi R_{\text{NS}}^2$,

$$L_{X\text{-ray}} = 4\pi R_{\text{NS}}^2 \sigma T^4, \quad (57)$$

where σ is the Stephan Boltzmann constant. However, there are important complications. One needs an accurate distance to the star in order to determine the absolute luminosity $L_{X\text{-ray}}$. E.g., one can identify a neutron star (NS) as a member of a globular star cluster of known distance. Equation 57 assumes a black body. There are important corrections to this from atmosphere models that may depend on composition and magnetic field (116). Finally, gravity is so strong that space is curved near a NS. If one observes the near face of a NS one also sees about 30% of the far face as light is bent around the star. Therefore, the effective surface area $4\pi R_{\text{NS}}^2$ actually depends on a mixture of radius and mass of the star (because the curvature of space depends on the mass). X-ray observations of NS radii by Ozel et al. (117), Guillot et al. (118), Steiner et al. (119), and Suleimanov et al. (120) yield a range of radii from $R_{\text{NS}} \approx 10$ km to more than 14 km. E.g., Steiner et al. infer $R_{\text{NS}} \approx 12$ km and, from the equation of state that they deduce from X-ray observations of NS, the neutron skin thickness in ^{208}Pb should be < 0.2 fm. The Large Observatory for Timing (LOFT) is a proposed European

Space Agency mission that should improve our knowledge of R_{NS} (121).

The neutron skin thickness in ^{208}Pb is also important for other properties of NS in addition to radii. E.g., the crust core transition density in a NS is correlated with ΔR (115). Finally, the interior composition and neutrino emissivity of a NS depends on the density dependence of the symmetry energy and ΔR (122).

5.4 Nuclear Experiments

In this subsection we briefly describe the nuclear experiments on ^{208}Pb (PREX and PREX II), ^{48}Ca (CREX), and on ^{12}C (see **Table 2**). PREX involved the scattering of 1 GeV electrons at about five degrees from a 0.5 mm thick ^{208}Pb target (17). The measured asymmetry,

$$A_{LR} = -0.656 \pm 0.060 \text{ (stat)} \pm 0.014 \text{ (syst)} \text{ ppm} , \quad (58)$$

involved a relatively small systematic error and a larger statistical error. From this measurement the weak form factor was deduced to be (123),

$$F_W(Q^2 = 0.0088 \text{ GeV}^2) = 0.204 \pm 0.028 , \quad (59)$$

and the root mean square radius of the weak charge distribution,

$$R_W = 5.826 \pm 0.181 \text{ fm} . \quad (60)$$

This can be directly compared to the well known (EM) charge radius of ^{208}Pb of 5.503 fm. This shows that the weak charge distribution of a heavy nucleus is more extended than the EM charge distribution. This is closely related to the expected neutron rich skin. By comparing predictions of A_{LR} for a range of relativistic mean field models, the neutron skin thickness is deduced to be (17),

$$\Delta R = R_n - R_p = 0.33_{-0.18}^{+0.16} \text{ fm} . \quad (61)$$

The error in ΔR is dominated by the statistical error in A_{LR} . This relatively large value for ΔR suggests that neutron stars should be relatively large $R_{\text{NS}} > 12$ km. However, the error bars are large. The goal of the approved PREX II experiment is to perform a second measurement of ^{208}Pb , at the same kinematics as PREX, in order to improve the statistical error on A_{LR} and deduce ΔR with a three times smaller error of ± 0.06 fm.

The CREX experiment aims to measure ΔR for ^{48}Ca to ± 0.02 fm (124). Like ^{208}Pb , ^{48}Ca is also a neutron rich nucleus with both closed proton and neutron shells (doubly magic). However ^{48}Ca is significantly lighter than ^{208}Pb . This allows microscopic coupled cluster calculations for ^{48}Ca (125) that are presently not feasible for ^{208}Pb . These calculations can relate ΔR to very interesting three neutron forces. Measuring ΔR for both the heavy ^{208}Pb and light ^{48}Ca will allow one to constrain isovector terms in the energy functional describing both surface (gradient) and volume energies.

Finally, a precision measurement of A_{LR} for ^{12}C can accurately constrain the weak charge of ^{12}C (126). The weak charge of ^{12}C involves the isoscalar combination of proton and neutron weak charges and constrains new physics in a way similar to the weak charge of Cs (as determined from APV). Because the atomic number of carbon is only 6, Coulomb distortion effects are small and can be accurately calculated. Furthermore, other nuclear structure corrections such as ΔR are also expected to be small at low momentum transfers. Therefore, a ^{12}C measurement should allow one to constrain the weak charge of a nucleus in a way that is free from atomic structure uncertainties that are important for APV.

To summarize, PVES from a nucleus can constrain the neutron skin thickness, $\Delta R = R_n - R_p$, and the density dependence of the symmetry energy. This is

important for nuclear structure. Furthermore, ΔR is important in astrophysics to constrain neutron star radii. Finally, both PVES and APV can constrain the weak charge of a nucleus.

6 PROBING NEW PHYSICS

PVES and related experiments can be used to search for evidence for new particles or interactions beyond those of the SM, or conversely to set exclusion limits. For example, new particles may modify the self-energies of the electroweak gauge bosons, leading to observable shifts in fundamental parameters such as $\sin^2 \theta_W$. This kind of effect is described by what are known as “oblique parameters”, and has been reviewed very recently in References (4, 9). But the new physics may also generate new quantum-mechanical amplitudes. These and other phenomena may be correlated in specific scenarios and their realizations in concrete models.

6.1 Beyond the SM Amplitudes and New Physics Scales

The NC Lagrangian in Equation 2 shows four-Fermi contact interactions normalized with respect to the EW scale, v . In the presence of non-standard physics there will be new contributions, so that e.g.,

$$\frac{g_{AV}^{eq}}{2v^2} \bar{e} \gamma^\mu \gamma^5 e \bar{q} \gamma_\mu q \rightarrow \left[\frac{g_{AV}^{eq}}{2v^2} + \frac{4\pi}{(\Lambda_{AV}^{eq})^2} \right] \bar{e} \gamma^\mu \gamma^5 e \bar{q} \gamma_\mu q, \quad (62)$$

and similarly for the other interaction types. In particular, new contact interactions are expected if leptons or quarks have a substructure and are composed of more fundamental objects, bound together by a new interaction of non-perturbative strength. Therefore, it has become conventional (127) to choose the new coefficients in 62 equal to 4π , and to parametrize the effects of the new operators in terms of compositeness scales Λ , but the resulting bounds can be rescaled

to apply to more general scenarios of new physics with strength $g_{\text{new}} \neq 4\pi$.

As an example, if one considers only models with positive- or negative-definite contributions (sometimes this sort of assumption is itself referred to as a model) then the constraint 9 implies, respectively, the 95% CL upper and lower limits,

$$|g_{VA}^{ee}|^+ = 0.0035 , \quad |g_{VA}^{ee}|^- = 0.0081 , \quad (63)$$

and one obtains,

$$\Lambda_+ > v \sqrt{\frac{8\pi}{|g_{VA}^{ee}|^+}} = 20.9 \text{ TeV} , \quad \Lambda_- > v \sqrt{\frac{8\pi}{|g_{VA}^{ee}|^-}} = 13.7 \text{ TeV} . \quad (64)$$

The MOLLER experiment is expected to achieve $\Delta g_{VA}^{ee} = 0.00052$ (2.3%) so that

$$\Lambda_{\pm}(\text{expected}) > v \sqrt{\frac{8\pi}{1.96 \Delta g_{VA}^{ee}}} = 38.7 \text{ TeV} . \quad (65)$$

For more general Lorentz and flavor structures it will be expedient to define compositeness scales that are directly comparable to those in 62. For example, when limits are quoted relative to an operator basis using left- and right-chiral fields, then both, the operators and their coefficients should be rotated so that the norm is preserved, i.e.,

$$\sum_{k,l=V,A} g_{kl}^2 = N \sum_{i,j=L,R} g_{ij}^2 , \quad (66)$$

with $N = 1$. However, the formalism of Reference (127) involving ordinary chiral projectors leads to a rescaling of couplings ($N = 4$) and of the compositeness scales (by a factor of 2). This appears to be the reason why the LEP 2 Collaborations (128) find generally much weaker limits for purely chiral operators.

A similar complication arises if a given experiment or data set is sensitive to some combination of quark flavors. As before, a rotated operator basis (without rescaling) should be used in which one of the operators coincides with the one relevant to the observable in question. It is the constraint on this operator, or

Table 4: Achieved (upper panel) or anticipated (lower panel) relative uncertainty, the corresponding tree level sensitivity to extract the weak mixing angle, and the expected reach to the associated compositeness scales (at 95% CL) for key parity violation experiments. For hadronic probes we also give the relevant linear combinations as the angle θ relative to $2g_{AV}^{eu} - g_{AV}^{ed}$.

	precision (%)	$\Delta \sin^2 \hat{\theta}_W(0)$	Λ_{new} [TeV]	θ
SLAC–E122	8.3	0.011	5.3	9.4°
SLAC–E122	110	0.44	0.9	99.4°
APV (^{205}Tl)	3.2	0.011	13.5	75.6°
APV (^{133}Cs)	0.58	0.0019	32.3	74.9°
SLAC–E158	14	0.0013	17.0	—
JLab–Qweak (run I)	19	0.0030	17.0	53.1°
JLab–Hall A	4.1	0.0051	7.8	26.2°
JLab–Hall A	61	0.051	2.9	116.2°
JLab–Qweak (final)	4.5	0.0008	33	53.1°
JLab–SoLID	0.6	0.00057	22	40.0°
JLab–MOLLER	2.3	0.00026	39	—
Mainz–P2	2.0	0.00036	49	53.1°
APV ($^{225}\text{Ra}^+$)	0.5	0.0018	34	75.7°
APV ($^{213}\text{Ra}^+ / ^{225}\text{Ra}^+$)	0.1	0.0037	16	55.5°
PVES (^{12}C)	0.3	0.0007	49	71.6°

equivalently the lower limit on the associated compositeness scale, which concrete models of new physics ought to satisfy. For example, elastic ep scattering probes

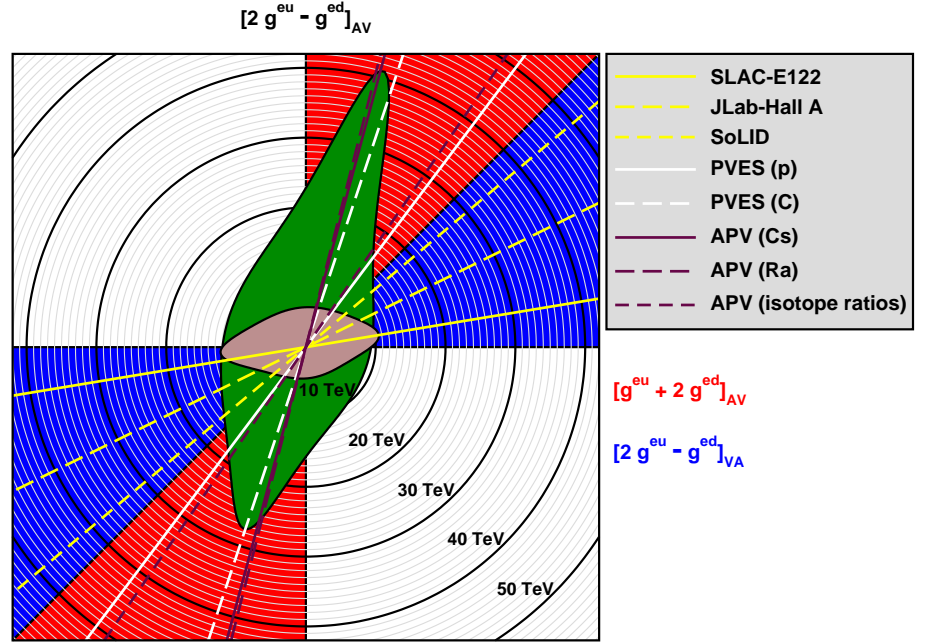


Figure 3: Compositeness scales for operators in the two planes (overlaid) defined by $g_{AV}^{eu} + 2g_{AV}^{ed}$ and $2g_{VA}^{eu} - g_{VA}^{ed}$ (vertical direction) vs. $2g_{AV}^{eu} - g_{AV}^{ed}$ (horizontal direction). The blue segment is accessible to PVDIS experiments (yellow lines) and defines a plane (containing the brown 95% CL exclusion contour) perpendicular to the plane containing the red segment, the green contour and the white and maroon lines. Thus, the two planes are subspaces of a three-dimensional parameter space which intersect along the horizontal direction. The lines indicate the coupling combinations of the various experiments relative to the common horizontal direction (cf. the angle θ shown in **Table 4**). Note that we have adjusted the E122 results for sea quark dilution ($R_v \neq 1$).

the operator,

$$\left[\frac{2g_{AV}^{eu} + g_{AV}^{de}}{\sqrt{5}} \right] \frac{\bar{e}\gamma^\mu\gamma^5 e}{2v^2} \left(\frac{2\bar{u}\gamma_\mu u + \bar{d}\gamma_\mu d}{\sqrt{5}} \right), \quad (67)$$

where the scale Λ_{AV}^{ep} may be defined such that the bracketed prefactor assumes

the fixed reference value 4π . Thus, the constraint 7 translates to

$$\Lambda_+ > v \sqrt{\frac{\sqrt{5} 8\pi}{|2g_{AV}^{eu} + g_{AV}^{ed}|^+}} = 15.3 \text{ TeV} , \quad \Lambda_- > 19.0 \text{ TeV} . \quad (68)$$

We summarize the current and expected compositeness scale limits from PVES and APV in **Table 4** and illustrate the scales in **Figure 3**.

6.2 Leptophobic Z' s

Leptophobic Z' s (129), corresponding to the class of models with additional neutral gauge bosons (Z') with negligible couplings to leptons, are particularly interesting in the context of PVES when they have sizable axial couplings to quarks. Large backgrounds from dijet production $p\bar{p}, pp \rightarrow jj$ in high energy hadron colliders, tend to dilute bounds on low mass leptophobic Z' s with $m_{Z'} \lesssim 300$ GeV. Planned precision measurements in electron-deuteron PVDIS can provide strong constraints precisely in this region of parameter space where hadron collider constraints are weakest.

Leptophobic Z' s with axial couplings to quarks typically generate sizable shifts in the g_{VA}^{eq} coefficients while the g_{AV}^{eq} are relatively unaffected. The latter are best measured by the Qweak, P2, and APV experiments and in A_{LR}^{DIS} in Equation 10 they can be treated as known quantities. SoLID is expected to measure the combination $2g_{VA}^{eu} - g_{VA}^{ed}$ with an uncertainty of about ± 0.007 , and is thus particularly well-suited to constrain such leptophobic Z' scenarios.

The dominant shift in the g_{VA}^{eq} coefficients arise (130) from γ - Z' mixing, as shown in **Figure 4**. Note that since the electron couplings are negligible, only quarks contribute to the $\Pi_{\gamma Z'}(q^2)$ two-point correlation function. In principle, Z - Z' mixing can also contribute, causing shifts in both the g_{AV}^{eq} and g_{VA}^{eq} coefficients. However, the Z - Z' mixing angle is constrained (131) to be less than 10^{-2} and

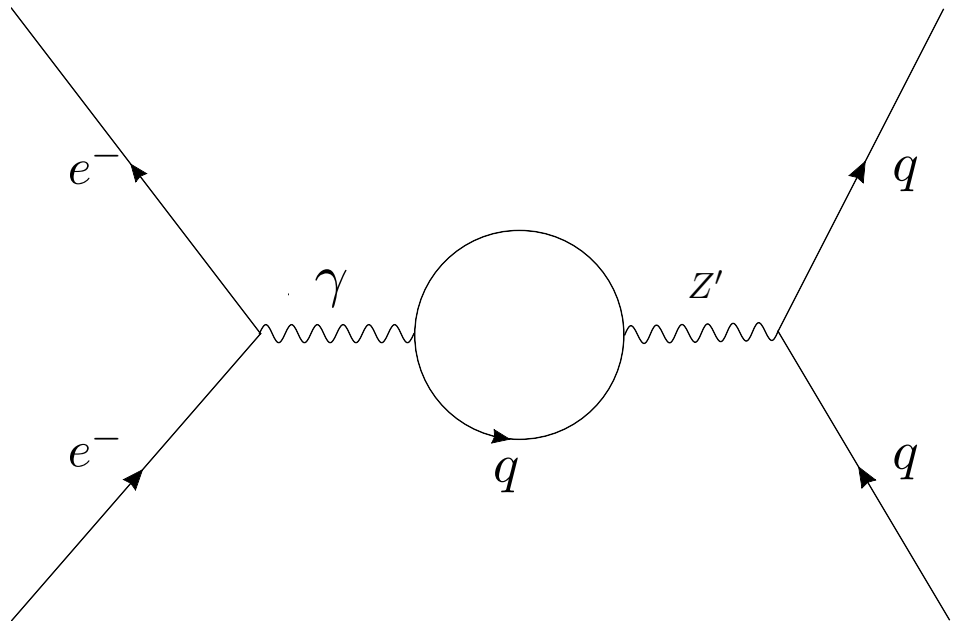


Figure 4: Dominant one-loop contribution of a leptophobic Z' to low energy parity violation. Note, that the Z' needs both vector and axial-vector couplings to produce this effect.

mostly affects the overall normalizations, so that this contribution is negligible.

The leptophobic Z' scenario explored in Reference (130) is expected to give rise to 3σ (6 to 7σ) effects in the combination $2g_{VA}^{eu} - g_{VA}^{ed}$ in the SoLID (EIC) experiments. This work was extended in Reference (132) to include vertex corrections from Z' loops, for the case where the Z' only couples to the light quarks which allows a systematic expansion in $m_q^2/m_{Z'}^2$. These analyses show that a large shift in the g_{VA}^{eq} coefficients, with the g_{AV}^{eq} relatively unaffected, would be a strong indication of a leptophobic Z' with axial-vector quark couplings.

6.3 Dark Z

The ‘‘Dark Z ’’ scenario (133, 134, 135) involves a light vector boson Z_d , with a mass in the range $10 \text{ MeV} < m_{Z_d} < 10 \text{ GeV}$, arising from a new spontaneously broken $U(1)_d$ gauge symmetry associated with a hidden sector which may or may not be related to dark matter. In contrast to other Z' scenarios, the physics of the Z_d cannot be integrated out and absorbed into contact interactions as long as $m_{Z_d}^2 \lesssim Q^2$; instead it has to be treated as a low mass dynamical degree of freedom. This is particularly interesting for low energy parity violation since there is an enhancement of the Z_d propagator relative to the Z propagator.

Before spontaneous symmetry breaking, the kinetic mixing term,

$$\mathcal{L}_{\text{kin.}} = \frac{\varepsilon}{2 \cos \theta_W} B_{\mu\nu} Z_d^{\mu\nu} , \quad (69)$$

gives rise to γ - Z_d and Z - Z_d mixing. The mixing parameter is constrained (136, 137, 138) to be $\varepsilon \lesssim 10^{-3}$ from studies of the so-called dark photon scenario (139, 140, 141), where charged particles couple to the Z_d by generating mixing with the photon.

More recently (133, 134, 135), the effects of the Z - Z_d mass mixing matrix were investigated. After spontaneous symmetry breaking, it has the general form

$$M_0 = m_Z^2 \begin{pmatrix} 1 & -\varepsilon_Z \\ -\varepsilon_Z & m_{Z_d}^2/m_Z^2 \end{pmatrix} , \quad \varepsilon_Z = \frac{m_{Z_d}}{m_Z} \delta , \quad (70)$$

where δ is a model-dependent quantity and the contribution from ε appears at $\mathcal{O}(\varepsilon^2)$ and is thus negligible. The constraint $0 \leq \delta^2 < 1$ is needed to avoid an infinite-range or tachyonic Z_d . The Z_d couples to the EM and weak neutral currents through,

$$\mathcal{L}_{\text{int.}} = -\frac{g}{\sqrt{2}} \left[\varepsilon J_A^\mu + \frac{\varepsilon_Z}{2 \cos \theta_W} J_Z^\mu \right] Z_{d\mu} . \quad (71)$$

The net effect of the new interactions in Equation 71 for PV amplitudes of the form $\mathcal{M}_{\text{NC}}^{\text{PV}} = v^{-2}F(\sin^2 \theta_W)/4$ is obtained through the replacements

$$\frac{1}{v^2} \rightarrow \frac{\rho_d}{v^2}, \quad \sin^2 \theta_W \rightarrow \kappa_d \sin^2 \theta_W, \quad (72)$$

where the quantities ρ_d and κ_d are given by,

$$\rho_d = 1 + \delta^2 \frac{m_{Z_d}^2}{Q^2 + m_{Z_d}^2}, \quad \kappa_d = 1 - \varepsilon \frac{m_Z}{m_{Z_d}} \delta \frac{\cos \theta_W}{\sin \theta_W} \frac{m_{Z_d}^2}{Q^2 + m_{Z_d}^2}. \quad (73)$$

As long as there are no accidental cancellations between the effects of ρ_d and κ_d , the strongest bound on the Z_d scenario, over its entire mass range, typically comes from APV. The shift in the Cs weak charge, Q_W^{Cs} , from its SM value is (133),

$$\Delta Q_W^{\text{Cs}} \approx \delta^2 \left[Q_W^{\text{Cs}}(\text{SM}) + 220 \frac{\varepsilon}{\varepsilon_Z} \cos \theta_W \sin \theta_W \right]. \quad (74)$$

For $\varepsilon \ll \varepsilon_Z$ one obtains the 90% CL bound, $\delta^2 \lesssim 0.006$. On the other hand, for $\varepsilon \simeq \varepsilon_Z$ a cancellation between the two terms above can dilute the bound. Independent but similar bounds (133) arise from Møller scattering (38, 13), primarily through its constraint on κ_d , for $\varepsilon \simeq \varepsilon_Z$ and $m_{Z_d}^2 \gg Q^2 \simeq (0.16 \text{ GeV})^2$. For very light masses, $m_{Z_d} \lesssim 200 \text{ MeV}$, the bound from Møller scattering is weaker than that from APV. However, there do exist regions in parameter space where Møller scattering can provide stronger bounds. E.g., for $\varepsilon \simeq 2 \times 10^{-3}$ and $m_{Z_d} \simeq 100 \text{ MeV}$, corresponding to the favored region to explain the observed discrepancy (142, 143, 144) in the muon anomalous magnetic moment, Møller scattering gives the bound $|\delta| < 0.01$. Ongoing and proposed experiments at JLAB (145, 10) and in Mainz (21) are expected to improve the bound by an order of magnitude.

Complementary constraints (133) arise from rare K and B meson decays, $K \rightarrow \pi Z_d$ and $B \rightarrow K Z_d$, respectively, through flavor changing neutral currents

mediated by the Z_d . The suppression factor m_{Z_d}/m_Z , from the induced coupling to the Z_d is overcome by the enhancement factors m_K/m_{Z_d} and m_B/m_{Z_d} in the longitudinally polarized Z_d channel. If the lifetime of the Z_d is long enough or if it decays as $Z_d \rightarrow \nu\bar{\nu}$ or to hidden sector particles, it will appear as a missing energy signal in these rare decays. Otherwise it can decay to $Z_d \rightarrow \ell^+\ell^-$ and appear as a displaced vertex. The pattern of Z_d decays is, of course, model dependent. The K -meson decays lead to constraints of the form $|\delta| \lesssim 0.01/\sqrt{\text{BR}(Z_d \rightarrow e^+e^-)}$ and $|\delta| \lesssim 0.001/\sqrt{\text{BR}(Z_d \rightarrow \text{missing energy})}$, where the overall numerical factor is model dependent. Similarly, the B -meson decays lead constraints of the form $|\delta| \lesssim 0.001/\sqrt{\text{BR}(Z_d \rightarrow e^+e^-)}$ and $|\delta| \lesssim 0.01/\sqrt{\text{BR}(Z_d \rightarrow \text{missing energy})}$.

Precision studies of Higgs decays at the LHC can also yield useful bounds (133) on the Z_d scenario. In particular, the $H \rightarrow ZZ_d$ mode can be constrained through studies of the $H \rightarrow ZZ^* \rightarrow \ell^+\ell^-\ell^+\ell^-$ and $H \rightarrow ZZ^* \rightarrow \ell^+\ell^-\nu\bar{\nu}$ channels. Just as for the rare K and B meson decays, the suppression factor of m_{Z_d}/m_Z from the induced coupling to the Z_d is overcome by an enhancement factor m_H/m_{Z_d} in the longitudinally polarized Z_d channel. For $m_H = 125$ GeV one typically finds the constraint $\Gamma(H \rightarrow ZZ_d)/\Gamma_H^{\text{SM}} \simeq 16\delta^2 \lesssim 0.1$. Eventually, with enough statistics, precision Higgs studies could yield useful independent bounds on δ .

Thus, low energy PV experiments can be used in concert with constraints coming from rare K , B and Higgs decays to study the Z_d scenario.

7 CONCLUSIONS

Many PVES experiments have been completed or are in various stages of progress. These experiments have a large physics reach, both in terms of the strong and weak interactions. They can search for physics beyond the standard model with

little theoretical uncertainty. In terms of a hypothetical compositeness scale, PVES experiments are among the most sensitive. They can also probe the dark sector at a low mass level, and search for a leptophobic Z' of intermediate mass.

PVES also provides a unique window on hadronic structure. For example, since the weak charge of the neutron is large, PVES experiments probe the radius of the density of neutrons in nuclei like ^{208}Pb and ^{48}Ca . In turn, this provides critical information for interpreting the physics of neutron stars. PVES can also study CSV at the parton level and provide a unique window to HT terms in DIS.

Acknowledgment

We thank Krishna Kumar for useful comments on the manuscript. J.E. acknowledges support by PAPIIT (DGAPA–UNAM) project IN106913, by CONACyT (México) project 151234, and by the Mainz Institute for Theoretical Physics (MITP). P.A.S. is funded in part by the Department of Energy (DOE) under grant DE-FG02-84ER40146. C.H. acknowledges support by DOE grants DE-FG02-87ER40365 (Indiana University) and de-sc0008808 (NUCLEI SciDAC Collaboration). S.M. is supported by Northwestern University.

LITERATURE CITED

1. SLAC–E122 Collab., Prescott CY, et al., *Phys. Lett.* B77:347 (1978).
2. SLAC–E122 Collab., Prescott CY, et al., *Phys. Lett.* B84:524 (1979).
3. Armstrong DS, McKeown RD, *Ann. Rev. Nucl. Part. Sci.* 62:337 (2012).
4. Kumar KS, Mantry S, Marciano WJ, Souder PA, *Ann. Rev. Nucl. Part. Sci.* 63:237 (2013).
5. Wood CS, et al., *Science* 275:1759 (1997).

6. Porsev SG, Beloy K, Derevianko A, Phys. Rev. Lett. 102:181601 (2009).
7. Dzuba VA, Berengut JC, Flambaum VV, Roberts B, Phys. Rev. Lett. 109:203003 (2012).
8. Ginges JSM, Flambaum VV, Phys. Rept. 397:63 (2004).
9. Erler J, Su S, Prog. Part. Nucl. Phys. 71:119 (2013).
10. Qweak Collab., Androic D, et al., Phys. Rev. Lett. 111:141803 (2013).
11. Cahn RN, Gilman FJ, Phys. Rev. D17:1313 (1978).
12. Derman E, Marciano WJ, Annals Phys. 121:147 (1979).
13. SLAC–E158 Collab., Anthony PL, et al., Phys. Rev. Lett. 95:081601 (2005).
14. MOLLER Collab., Mammei J, Nuovo Cim. C035N04:203 (2012).
15. JLab PVDIS Collab., Zheng X, et al., Nature 506:67 (2014) .
16. Accardi A, et al., Electron Ion Collider: The Next QCD Frontier — Understanding the glue that binds us all, arXiv:1212.1701 [nucl.ex].
17. PREX Collab., Abrahamyan S, et al., Phys. Rev. Lett. 108:112502 (2012).
18. Alcorn J, et al., Nucl. Instrum. Meth. A522:294 (2004).
19. Souder PA, et al., Phys. Rev. Lett. 65:694 (1990).
20. Souder P, Conf. Proc. C0804071:243 (2008).
21. P2 Collab., Becker D, et al., PoS Bormio 2013:024 (2013).
22. A4 Collab., Baunack S, et al., Phys. Rev. Lett. 102:151803 (2009).
23. SAMPLE Collab., Spayde DT, et al., Phys. Rev. Lett. 84:1106 (2000).
24. Souder PA, Holmes R, New spectrometers for precision measurements of parity violation with polarized electrons, Proc. *Parity violation in electron scattering*, Pasadena, CA, Feb. 23–24, 1990, pp. 137–151 (World Scientific).
25. Heil W, et al., Nucl. Phys. B327:1 (1989).
26. HAPPEX Collab., Aniol KA, et al., Phys. Rev. C69:065501 (2004).

27. GØ Collab., Armstrong DS, et al., Phys. Rev. Lett. 95:092001 (2005).
28. HAPPEX Collab., Acha A, et al., Phys. Rev. Lett. 98:032301 (2007).
29. Sinclair CK, et al., Phys. Rev. ST Accel. Beams 10:023501 (2007).
30. Adderley PA, et al., Phys. Rev. ST Accel. Beams 13:010101 (2010).
31. Kumar KS, Souder PA, Prog. Part. Nucl. Phys. 45:S333 (2000).
32. Chudakov E, Luppov V, IEEE Trans. Nucl. Sci. 51:1533 (2004).
33. Marciano WJ, Sirlin A, Phys. Rev. D27:552 (1983).
34. Marciano WJ, Sirlin A, Phys. Rev. D29:75 (1984).
35. Czarnecki A, Marciano WJ, Phys. Rev. D53:1066 (1996).
36. Erler J, Kurylov A, Ramsey-Musolf MJ, Phys. Rev. D68:016006 (2003).
37. Veltman MJG, Nucl. Phys. B123:89 (1977).
38. Czarnecki A, Marciano WJ, Int. J. Mod. Phys. A15:2365 (2000).
39. Erler J, Ramsey-Musolf MJ, Phys. Rev. D72:073003 (2005).
40. Zykunov VA, Suarez J, Tweedie BA, Kolomensky YG, First order QED corrections to the parity-violating asymmetry in Møller scattering, arXiv:hep-ph/0507287.
41. Arbuzov A, et al., Comput. Phys. Commun. 94:128 (1996).
42. SoLID Collab., Souder PA, AIP Conf. Proc. 1441:123 (2012).
43. Erler J, Phys. Rev. D59:054008 (1999).
44. Davier M, Hoecker A, Malaescu B, Zhang Z, Eur. Phys. J. C71:1515 (2011).
45. Blunden P, Melnitchouk W, Thomas A, Phys. Rev. Lett. 109:262301 (2012).
46. Gorchtein M, Horowitz CJ, Phys. Rev. Lett. 102:091806 (2009).
47. Rislow BC, Carlson CE, Phys. Rev. D88:013018 (2013).
48. Gorchtein M, Horowitz C, Ramsey-Musolf MJ, Phys. Rev. C84:015502 (2011).

49. Hall NL, et al., Phys. Rev. D88:013011 (2013).
50. Gorchtein M, et al., Theory Uncertainty in Extracting the Proton's Weak Charge: White Paper, arXiv:1311.4586 [hep-ph].
51. Young RD, Carlini RD, Thomas AW, Roche J, Phys. Rev. Lett. 99:122003 (2007).
52. Kwiatkowski A, Spiesberger H, Möhring HJ, Comput. Phys. Commun. 69:155 (1992).
53. Aleksejevs A, Barkanova S, Kuraev E, Zykunov V, PoS ICHEP 2012:470 (2013).
54. Bjorken JD, Phys. Rev. D18:3239 (1978).
55. Wolfenstein L, Nucl. Phys. B146:477 (1978).
56. Fajfer S, Oakes RJ, Phys. Rev. D30:1585 (1984).
57. Castorina P, Mulders PJ, Phys. Rev. D31:2760 (1985).
58. Dasgupta M, Webber BR, Phys. Lett. B382:273 (1996).
59. Stein E, Meyer-Hermann M, Mankiewicz L, Schäfer A, Phys. Lett. B376:177 (1996).
60. Signal AI, Nucl. Phys. B497:415 (1997).
61. Stein E, Maul M, Mankiewicz L, Schäfer A, Nucl. Phys. B536:318 (1998).
62. Beneke M, Phys. Rept. 317:1 (1999).
63. Hobbs T, Melnitchouk W, Phys. Rev. D77:114023 (2008).
64. Mantry S, Ramsey-Musolf MJ, Sacco GF, Phys. Rev. C82:065205 (2010).
65. Ellis RK, Furmanski W, Petronzio R, Nucl. Phys. B212:29 (1983).
66. Ji XD, Nucl. Phys. B402:217 (1993).
67. Qiu JW, Phys. Rev. D42:30 (1990).
68. Chodos A, et al., Phys. Rev. D9:3471 (1974).

69. Bolz J, Kroll P, *Z. Phys.* A356:327 (1996).
70. Diehl M, Feldmann T, Jakob R, Kroll P, *Eur. Phys. J.* C8:409 (1999).
71. Braun VM, Lautenschläger T, Manashov AN, Pirnay B, *Phys. Rev.* D83:094023 (2011).
72. Belitsky AV, Manashov A, Schäfer A, *Phys. Rev.* D84:014010 (2011).
73. Seng CY, Ramsey-Musolf MJ, *Phys. Rev.* C88:015202 (2013).
74. Martin AD, Roberts RG, Stirling WJ, Thorne RS, *Eur. Phys. J.* C35:325 (2004).
75. Martin AD, Roberts RG, Stirling WJ, Thorne RS, *Eur. Phys. J.* C39:155 (2005).
76. Glück M, Jimenez-Delgado P, Reya E, *Phys. Rev. Lett.* 95:022002 (2005).
77. Sather E, *Phys. Lett.* B274:433 (1992).
78. Londergan JT, et al., *Phys. Lett.* B340:115 (1994).
79. Boros C, Steffens FM, Londergan JT, Thomas AW, *Phys. Lett.* B468:161 (1999).
80. Londergan JT, Peng JC, Thomas AW, *Rev. Mod. Phys.* 82:2009 (2010).
81. Llewellyn Smith CH, *Phys. Lett.* B128:107 (1983).
82. Bickerstaff RP, Thomas AW, *J. Phys.* G15:1523 (1989).
83. Ericson M, Thomas AW, *Phys. Lett.* B128:112 (1983).
84. Jaffe RL, *Phys. Rev. Lett.* 50:228 (1983).
85. Alde DM, et al., *Phys. Rev. Lett.* 64:2479 (1990).
86. Saito K, Michels A, Thomas AW, *Phys. Rev.* C46:2149 (1992).
87. Weinstein LB, et al., *Phys. Rev. Lett.* 106:052301 (2011).
88. Kang ZB, Liu X, Mantry S, Qiu JW, *Phys. Rev.* D88:074020 (2013).
89. Kang ZB, Mantry S, Qiu JW, *Phys. Rev.* D86:114011 (2012).

90. Kang D, Lee C, Stewart IW, Phys. Rev. D88:054004 (2013).
91. Kang ZB, Liu X, Mantry S, The 1-Jettiness DIS event shape: NNLL + NLO results, arXiv:1312.0301 [hep-ph].
92. Stewart IW, Tackmann FJ, Waalewijn WJ, Phys. Rev. Lett. 105:092002 (2010).
93. European Muon Collab., Aubert JJ, et al., Phys. Lett. B123:275 (1983).
94. Cloët IC, Bentz W, Thomas AW, Phys. Rev. Lett. 109:182301 (2012).
95. Souder PA, AIP Conf. Proc. 747:199 (2005).
96. Saito K, et al., Phys. Lett. B493:288 (2000).
97. Afnan IR, et al., Phys. Rev. C68:035201 (2003).
98. Frankfurt LL, Strikman MI, Phys. Rept. 76:215 (1981).
99. Simula S, Phys. Lett. B387:245 (1996).
100. Melnitchouk W, Sargsian M, Strikman MI, Z. Phys. A359:99 (1997).
101. Melnitchouk W, Afnan IR, Bissey FRP, Thomas AW, Phys. Rev. Lett. 84:5455 (2000).
102. Whitlow LW, et al., Phys. Lett. B250:193 (1990).
103. Tung WK, et al., JHEP 0702:053 (2007).
104. Melnitchouk W, Thomas AW, Phys. Lett. B377:11 (1996).
105. Melnitchouk W, Peng JC, Phys. Lett. B400:220 (1997).
106. Horowitz CJ, Pollock SJ, Souder PA, Michaels R, Phys. Rev. C63:025501 (2001).
107. Horowitz CJ, Piekarewicz J, Phys. Rev. C86:045503 (2012).
108. Breton V, et al., Phys. Rev. Lett. 66:572 (1991).
109. Horowitz CJ, Phys. Rev. C57:3430 (1998).
110. Kortelainen M, et al., Phys. Rev. C88:031305 (2013).

111. Roca-Maza X, Centelles M, Viñas X, Warda M, Phys. Rev. Lett. 106:252501 (2011).
112. Tsang MB, et al., Phys. Rev. C86:015803 (2012).
113. Typel S, Brown BA, Phys. Rev. C64:027302 (2001).
114. Horowitz CJ, Piekarewicz J, Phys. Rev. C64:062802 (2001).
115. Horowitz CJ, Piekarewicz J, Phys. Rev. Lett. 86:5647 (2001).
116. Suleimanov V, Poutanen J, Werner K, A&A 545:A120 (2012).
117. Özel F, Rept. Prog. Phys. 76:016901 (2013).
118. Guillot S, Servillat M, Webb NA, Rutledge RE, ApJ 772:7 (2013).
119. Lattimer JM, Steiner AW, Neutron Star Masses and Radii from Quiescent Low-Mass X-ray Binaries, arXiv:1305.3242 [astro-ph.HE].
120. Suleimanov V, Poutanen J, Revnivtsev M, Werner K, ApJ 742:122 (2011).
121. Bozzo E, et al., The LOFT mission: new perspectives in the research field of (accreting) compact objects, arXiv:1312.1697 [astro-ph.IM].
122. Horowitz CJ, Piekarewicz J, Phys. Rev. C66:055803 (2002).
123. Horowitz CJ, et al., Phys. Rev. C85:032501 (2012).
124. CREX Collab., Mammei J, et al., *CREX: Parity-violating Measurement of the weak charge distribution of ^{48}Ca to 0.02 fm Accuracy*, JLab Proposal. http://hallaweb.jlab.org/parity/prex/c-rex2013_v7.pdf.
125. Hagen G, et al., Phys. Rev. Lett. 109:032502 (2012).
126. Moreno O, Donnelly TW, Nuclear Structure Uncertainties in Parity-Violating Electron Scattering from Carbon 12, arXiv:1311.1843 [nucl-th].
127. Eichten E, Lane KD, Peskin ME, Phys. Rev. Lett. 50:811 (1983).
128. ALEPH, DELPHI, L3, OPAL Collab., LEP Electroweak Working Group, Schael S, et al., Phys. Rept. 532:119 (2013).

129. Babu KS, Kolda CF, March-Russell J, Phys. Rev. D54:4635 (1996).
130. Buckley MR, Ramsey-Musolf MJ, Phys. Lett. B712:261 (2012).
131. Erler J, Langacker P, Munir S, Rojas E, JHEP 0908:017 (2009).
132. Gonzalez-Alonso M, Ramsey-Musolf MJ, Phys. Rev. D87:055013 (2013).
133. Davoudiasl H, Lee HS, Marciano WJ, Phys. Rev. D85:115019 (2012).
134. Davoudiasl H, Lee HS, Marciano WJ, Phys. Rev. Lett. 109:031802 (2012).
135. Davoudiasl H, Lee HS, Marciano WJ, Phys. Rev. D86:095009 (2012).
136. Batell B, Pospelov M, Ritz A, Phys. Rev. D79:115008 (2009).
137. Bjorken JD, Essig R, Schuster P, Toro N, Phys. Rev. D80:075018 (2009).
138. Jaeckel J, Ringwald A, Ann. Rev. Nucl. Part. Sci. 60:405 (2010).
139. Fayet P, Phys. Lett. B95:285 (1980).
140. Fayet P, Phys. Lett. B96:83 (1980).
141. Fayet P, Mezard M, Phys. Lett. B104:226 (1981).
142. Muon G-2 Collab., Bennett GW, et al., Phys. Rev. D73:072003 (2006).
143. Fayet P, Phys. Rev. D75:115017 (2007).
144. Pospelov M, Phys. Rev. D80:095002 (2009).
145. McKeown RD, AIP Conf. Proc. 1423:289 (2012).